JOM, Vol. 64, No. 7, 2012
DOI: 10.1007/s11837-012-0360-y

Relating Dynamic Properties to Atomic Structure in Metallic Glasses

H. W. SHENG,[1,5] E. MA,[2] and M. J. KRAMER[3,4]

1.—School of Physics, Astronomy and Computational Sciences, George Mason University, Fairfax, VA 22030, USA. 2.—Department of Materials Science and Engineering, Johns Hopkins University, Baltimore, MD 22018, USA. 3.—Ames Laboratory, U.S. Department of Energy, Ames, IA 50011, USA. 4.—Department of Materials Science and Engineering, Iowa State University, Ames, IA 50011, USA. 5.—e-mail: hsheng@gmu.edu

Atomic packing in metallic glasses is not completely random but displays various degrees of structural ordering. While it is believed that local structures profoundly affect the properties of glasses, a fundamental understanding of the structure–property relationship has been lacking. In this article, we provide a microscopic picture to uncover the intricate interplay between structural defects and dynamic properties of metallic glasses, from the perspective of computational modeling. Computational methodologies for such realistic modeling are introduced. Exploiting the concept of quasi-equivalent cluster packing, we quantify the structural ordering of a prototype metallic glass during its formation process, with a new focus on geometric measures of subatomic "voids." Atomic sites connected with the voids are found to be crucial in terms of understanding the dynamic, including vibrational and atomic transport, properties. Normal mode analysis is performed to reveal the structural origin of the anomalous boson peak (BP) in the vibration spectrum of the glass, and its correlation with atomic packing cavities. Through transition-state search on the energy landscape of the system, such structural disorder is found to be a facilitating factor for atomic diffusion, with diffusion energy barriers and diffusion pathways significantly varying with the degree of structural relaxation/ordering. The implications of structural defects for the mechanical properties of metallic glasses are also discussed.

INTRODUCTION

When metallic liquids are cooled, atoms gradually lose their kinetic energy and their motion becomes increasingly sluggish as the temperature decreases. If the liquids can avoid crystallization, they will eventually be kinetically arrested into a glassy state.[1–7] The lack of periodicity of atomic arrangements in metallic liquids and their glasses (MGs) makes their structure notoriously difficult to characterize, leaving many open questions unanswered in this area.[6,7] In a broader picture, there are two fundamental questions we wish to address: Are we able to provide a universal and unique structural description for MGs? And how do we establish quantitative relationships between the structure and properties of MGs?

Metallic liquids, though lacking order, do exhibit interatomic distances within a narrow distribution. As these liquids cool into the glassy state, they tend to form lower-energy local clusters. This has been known as topological short-range ordering (SRO).[8–11] One typical example is the hypothesis of icosahedral clusters in metallic mercury, as predicted by Frank[12] half a century ago. The formation of icosahedral clusters in glasses is called icosahedral short-range order (ISRO).[13–15] Over the years, much progress has been made in terms of understanding the SRO of MGs. In addition to ISRO, we now know that MGs may exhibit other types of SRO, depending on the chemistry of the system;[16–18] For instance, in the transition metal–metalloid (TM–M) MG Pd-Si, the tricapped trigonal prism (TTP) type of SRO may be dominant.[10,16,19] Knowledge of SRO is fundamental because it can be regarded as the basic building unit for MGs, and larger structural organizations on the medium range (a few atomic shells) are spatial extensions of SRO.[16,17,20]

(Published online July 18, 2012)

Meanwhile, many physical properties are very sensitive to SRO, such as atomic packing density,[20–24] electron, magnetic, and x-ray spectroscopy,[25–28] etc. While much recent interest has extended to the structural order beyond the short range, our understanding of the short-range structure of glasses is still far from being complete.

The details of atomic packing on the atomic level influence materials properties. This is evidenced from the fact that thermal annealing leads to a wide spectrum of property changes of MGs, such as density, enthalpy, mechanical properties, diffusivity, magnetic suitability, etc.[29–33] These property changes can be ascribed to internal structural ordering. Recent research shows that MG properties have more intricate relationships with the structural features of MGs, typical examples being the mechanical behavior and relaxation dynamics of glasses, which may be related to the structural heterogeneity in MGs.[34–37] Many phenomenological theories, e.g., the free-volume theory[38–41] among others, are able to relate macroscopic properties of MGs with structure by introducing some order parameters, built upon the premise that local atomic-level structure has quantifiable responses to external perturbations. Microscopically, although recent advances in experiments[42–44] have enabled us to probe the structural origin of the properties of metallic glasses down to the nanometer scale, the exact relationships between the local structures and properties of MGs have not been clear. As such, there is a pressing need to establish a microscopic picture describing the correlations between atomic packing and the properties of metallic glasses.

Naturally, when we speak of structural order in glasses, e.g., short- to medium-range order, what is left unsaid is that there is structural disorder in the material. Quantification of structural defects, as an alternative view of structural order, will provide complementary but sometimes more revealing information about the structure of metallic glasses. Unfortunately, knowledge on structural defects of MGs has been very limited. Just as it is difficult to quantify structural order in amorphous solids, it is also difficult to quantify structural defects. Unlike crystalline materials, where defects can be precisely defined as point and line defects, in amorphous solids there is no unambiguous definition of structural defects because an ideal amorphous structure is not experimentally accessible.[45,46] One workaround is to take the existing amorphous model and analyze atomic packing imperfections trapped in the structure.[32] In the free-volume theory, the dilation and compressed area were introduced for the identification of defects.[39] Similarly, in the atomic-level stresses treatment introduced by Egami,[47–51] atomic defects are defined based on atomic volume strain.

To follow up our previous work[16] on the short- to medium-range order in MGs, in this article, we report our recent progress on the structural aspect of glasses, accentuating the features of subatomic voids. We illustrate how these structural defects profoundly affect the dynamic properties of glasses. Two fundamental dynamic properties will be considered in this article, namely vibration properties and atomic transport properties.

The article is organized as follows: In "Formation of the $Ni_{80}P_{20}$ Metallic Glass" and "Short- to Medium-Range Order in the Metallic Glass" sections, we first establish a reliable MG model to expatiate on the concept of short- to medium-range order in MGs. New insight will be provided regarding atomic packing features of nonicosahedral SRO. In "Subatomic Voids as Structure Defects in Metallic Glasses" section, we focus on the quantification of subatomic voids in MGs, and provide properties of the subatomic voids in MGs. In "Vibrational Properties and Structural Defects" and "Atomic Diffusion Mechanisms and Structural Defects" sections, we correlate dynamic properties of MGs with atomic packing defects. More specifically, we uncover the structural origin for the BP, and provide micromechanisms for atomic diffusion in MGs. Lastly, in "Mechanical Properties and Structural Defects" section, we briefly discuss how structural disorder is related to deformation mechanisms.

COMPUTATIONAL APPROACHES FOR METALLIC GLASS SIMULATION

Previously, in solving the structure of metallic glasses,[16] we resorted to the combination of reverse Monte Carlo (RMC) and ab initio molecular dynamics (MD) methods. Here, we overcome some limitations encountered with the RMC and ab initio methods, and employ large-scale classical MD to simulate the structural evolution of metallic glasses over extended spatial and temporal scales that cannot be achieved by ab initio MD or RMC. The success of this method, i.e., extraction of real structural features of MGs, largely depends on how reliable the interatomic potentials are. Therefore, our first goal is to develop robust and high-quality interatomic potentials that can accurately describe the metallic systems. In the past, there have been methods proposed to build efficient pairwise potentials from first-principles Hamiltonians, such as the nearly free-electron tight-binding approach[51,52] by Hausleitner and Hafner. This method is appealing because of its simplicity and physical underpinnings in quantum mechanics. However, we opted for a newer method which may offer better accuracy for potential development. In our approach we used the embedded-atom-method formalism (EAM)[53–56] to represent interatomic interactions. Large first-principles databases were established[57,58] to span a wide phase space of the system and then were combined with experimental data to extract EAM interatomic potentials. Since our mindset was to build computational models that reflect the physical

properties of real materials, during potential fitting, the physical meaning of each parameter was not the primary concern. The EAM parameters were treated as mathematical entities and were allowed to vary to produce best matches between EAM and first-principles calculations. Using this method we have developed a number of high-quality interatomic potentials for simulations of metallic glasses and liquids.[19,58,59] An example for the potential development is given in the Appendix.

In this work, the prototype MG former Ni-P is used as an example to illustrate structural ordering in MGs and its correlations with dynamic properties. Selection of this system is to make contact with our original work related to the concept of quasi-equivalent cluster packing. Further, a vast literature regarding liquid dynamics and the glass transition has used a putative potential model based on the $Ni_{80}P_{20}$ system developed by Kob and Andersen, i.e., the binary mixture Lennard–Jones (BMLJ) model.[60–65] Our results in this work can thus be linked with established results on the BMLJ model for critical comparison. For the structure and phase diagram of the BMLJ model, the reader may refer to Refs. [66–68]. Early computer simulations on the Ni-P system employing other types of pair potential can also be found in literature.[52,69–71]

FORMATION OF THE $Ni_{80}P_{20}$ Metallic Glass

Classical MD employing the EAM potential was performed to generate $Ni_{80}P_{20}$ metallic glasses on the computer. Figure 1 shows the MD simulation results of the formation of $Ni_{80}P_{20}$ glass with 32,000 atoms (~7.8 nm in each direction), cooled under constant pressure and periodic boundary conditions, with cooling rates varying from 10^4 K/ns to 10 K/ns.

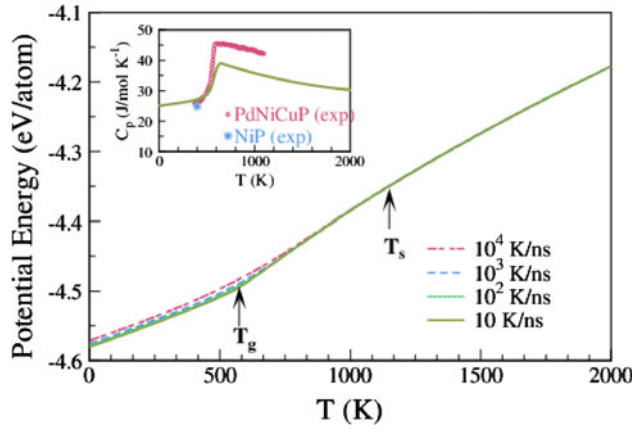

Fig. 1. Potential energy as a function of temperature for the formation of $Ni_{80}P_{20}$ metallic glass. The inset shows the specific heat of the Ni-P MG cooled with a cooling rate of 10 K/ns. T_g denotes the glass-transition temperature of the Ni-P MG. The onset dynamic slowing-down temperature of the liquid is estimated to be $T_s \approx 1200$ K based on the super-Arrhenius relaxation behavior of the liquid. Experimental data for the specific heat of PdNiCuP are taken from Ref. 72 and for Ni-P from Ref. 73

The slowest cooling rate (10 K/ns) is comparable to that of vapor deposition in experiment. During the cooling process, the potential energy of the system decreases with decreasing temperature. Slow cooling rates lead to glasses with low potential energy. However, the energy difference between the MGs cooled at 100 K/ns and 10 K/ns is found to be only 2 meV/atom at 300 K. Our structural analysis will mainly be conducted on the system quenched with the slowest cooling rate (10 K/ns). The shape of the potential energy curve can be further revealed from the specific heat derived from the derivative of enthalpy with respect to temperature (dH/dT). In the inset of Fig. 1, the derived specific heat of the Ni-P MG (10 K/ns) is plotted against temperature. The shape of the specific heat versus temperature for the Ni-P glass is typical, bearing close similarity to the experimental specific heat curve of Pd-Ni-Cu-P.[72] Similar specific heat behavior was reported for other binary glass formers recently[19] in computer simulation and was linked to their internal structural changes. In the glassy state, the specific heat of the simulated Ni-P MG compares favorably with the experimental data of Ni-P MG (24.9 J/K-mol at 400 K[73]). The glass-transition temperature $T_g \approx 575$ K was estimated from the departure of the potential energy from its linear relationship with temperature. This T_g is slightly lower than that of the real-world $Ni_{80}P_{20}$ MG at ~596 K to 630 K.[74,75] We also identified the onset dynamic slowing-down temperature (T_s) for the Ni-P liquid, as labeled on the potential energy curve (analysis on the liquid dynamics of the system is not presented herein). The density of the computer-generated glass is 7.95 g/cm^3 at 300 K, which is close to the density of electrodeposited $Ni_{80}P_{20}$ metallic glass (7.97 g/cm^3).[76]

The two-body radial distribution function (RDF) $g(r)$ of the Ni-P system is plotted in Fig. 2 to demonstrate how the internal structure evolves during the cooling process. The main peaks in the RDFs gradually shift toward short distances, while their intensities increase with decreasing temperature. One prominent feature of the RDFs is that the second peaks split below a certain temperature, denoted as T_p, which lies between T_s and T_g, suggesting that important internal structural changes occur in the liquid during supercooling. In fact, this peak-splitting phenomenon may be correlated with the percolation of locally ordered structures[39,77] of the supercooled liquid. Details of the structural ordering are analyzed in the next section.

At room temperature, the RDFs of the simulated glass can be compared with experimental ones extracted from scattering exteriments.[78,79] We directly compare the structural factor of the glass with that obtained from synchrotron x-ray radiation as shown in Fig. 3. The experimental x-ray structure factor was optimized from the x-ray diffraction data (see, e.g., Ref. 80, for the optimization process). In simulation, the total x-ray structure factor was calculated based on

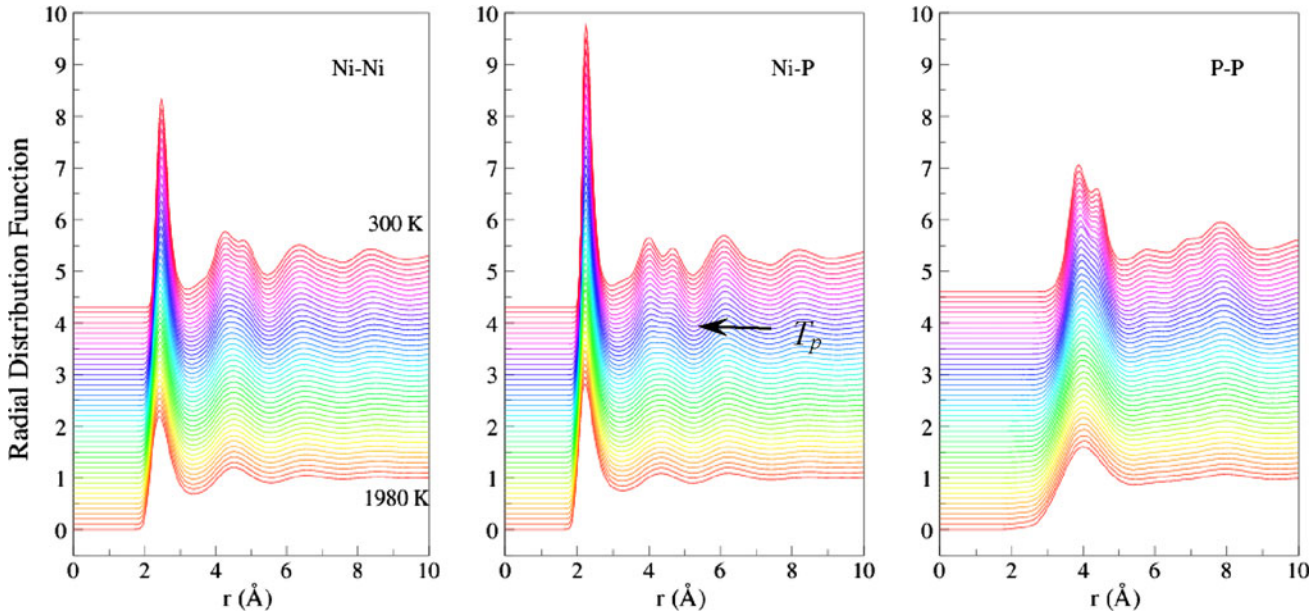

Fig. 2. RDF of the Ni-P MG cooled with a cooling rate of 10 K/ns. The arrow indicates the temperature at which the peak split becomes obvious ($T_p \approx 700$ K). Note on the P-P partial RDFs that the first peak is absent due to solute–solute avoidance.

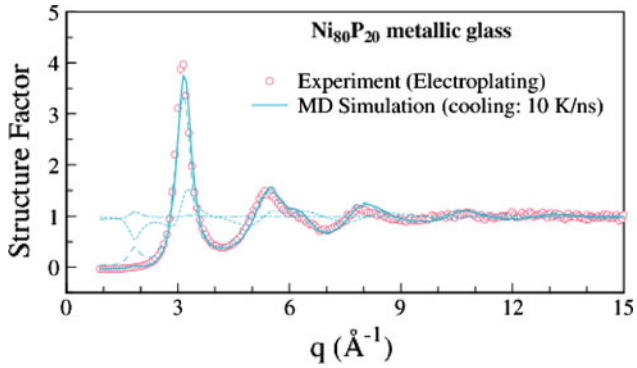

Fig. 3. Comparison between experimental and simulated x-ray structure factors. The dashed lines are computed partial structure factors.

$$S(q) = \sum_{\alpha}\sum_{\beta} \frac{c_\alpha c_\beta f_\alpha f_\beta}{\left(\sum_\alpha c_\alpha f_\alpha\right)^2} S_{\alpha\beta}(q), \qquad (1)$$

where c_α and c_β are the concentration of the alloy, f_α and f_β are the atomic scattering factors, and q is the scattering momentum transfer. $S_{\alpha\beta}(q)$ is the partial structure factor related to species α and β and can be calculated from the RDFs via Fourier transformation as

$$S_{\alpha\beta} = \sum_{\alpha}\sum_{\beta} = \frac{4\pi\rho}{q}\int_0^\infty r\left[g_{\alpha\beta}(r) - 1\right]\sin(qr)\mathrm{d}r, \qquad (2)$$

where ρ is the density of the system. The comparison of the computed and experimental structure factors is shown in Fig. 3. After taking into account the effect of cooling rate, satisfactory agreement can be found between simulated and experimental structure factors, including peak position, intensity, and shape. Not surprisingly, the partial RDFs of the computer-generated MG match very well with experimental and ab initio results (not shown). Justified by the above validation and comparison, we now proceed to use the computational model to simulate the structure and dynamic properties of the real-world MG.

SHORT- TO MEDIUM-RANGE ORDER IN THE METALLIC GLASS

The concept of quasi-equivalent cluster packing[16] was previously proposed to explain the short- to medium-range structure of solute-lean MGs. In this concept, solute-centered atoms have the tendency to form well-ordered coordination polyhedra (i.e., Kasper polyhedra[10,16,81,82]), and the main type is determined by the size ratio of the solvent atom and the solute atom of the system. The coordination polyhedra are considered as "quasi-equivalent clusters" and serve as building blocks for large structural organizations in the medium range. Here, we re-examine this structural picture with large-scale MD simulation and shed light on new features associated with this atomic packing model.

Locally Preferred Kasper Polyhedra

For TM–M glasses, due to the strong interactions between metal and metalloid atoms, a well-known phenomenon is the so-called solute–solute avoidance,[32] where solute atoms tend to avoid each other, promoting bonding between unlike atoms.

Consequently, solute atoms are surrounded by solvent atoms only. This phenomenon has been captured in our simulation, exemplified by the complete disappearance of the first peak in the partial RDF of the solute–solute pair, as shown in Fig. 2. Solute–solute avoidance is also indicative of strong chemical SRO, which can be characterized by the generalized Warren CSRO parameter[83,84] defined as

$$\alpha_W = Z_{cc}/Z_W, \quad (3)$$

$$Z_{cc} = x_B(Z_{AA} - Z_{BA}) + (1 - x_B)(Z_{BB} - Z_{AB}), \quad (4)$$

$$Z_W = x_B Z_A + (1 - x_B)Z_B, \quad (5)$$

where Z_{AB} is the partial coordination number (CN) of B atoms around A, Z_A is the total CN around A, and x_B is the nominal composition of B. A negative α_{AB} means that unlike bonds are favored. In the current case, $\alpha_W = -0.17$ indicates strong interactions between Ni and P, promoting formation of solute-centered clusters. This value is in good agreement with the experimental value of $\alpha_W = -0.153$[84] for the $Ni_{80}P_{20}$ glass.

The topology of solute-centered clusters was analyzed by the Voronoi spatial tessellation technique.[16,85,86] These clusters can be grouped according to their Voronoi indices $\langle n_3, n_4, n_5, n_6\rangle$, where the numbers in the bracket n_i denote the number of i-edged faces of the Voronoi cell associated with the particular coordination polyhedron. The sum of n_i equals the CN of the center atom. The Voronoi index can be used to differentiate different types of coordination polyhedra. The distributions of CN and coordination polyhedron type around solute atoms are shown in Fig. 4. We start from the anatomy of CN around the solute atoms.

For the computer-generated Ni-P glass, the average CN around P is 10.3 ± 0.3 (the error margin coming from different criteria used to remove small faces and edges from the Voronoi construction) with the Voronoi method. The CN distribution of P mainly falls on CN = 9, 10, and 11. Generally speaking, the average CN is determined by the effective size ratio, R^*, between the solute atom and the solvent atom.[16,21,87] Large solute atoms accommodate more solvent atoms in the first coordination shell, whereas small solute atoms accommodate fewer solvent atoms in the first coordination shell. Ideal icosahedral (CN = 12) and bicapped square antiprism (CN = 10) atomic packing correspond to size ratios of 0.902 and 0.835, respectively,[16] between the center atom and the surrounding atom. In the case of Ni-P, the effective size ratio between Ni and P was estimated by the formula $(D_{Ni\text{-}P} - D_{Ni\text{-}Ni}/2)/(D_{Ni\text{-}Ni}/2)$, where D_{Ni-Ni} and D_{Ni-P} are the bond distances between Ni-Ni (2.48 Å) and Ni-P (2.25 Å) pairs, obtained from the RDFs in Fig. 2. The effective size ratio between P and Ni is estimated to be 0.82, suggesting that the P atom can accommodate 10 Ni atoms as its first neighbors. Given the "soft sphere" nature of the atomic bonding between Ni and P, it is thus reasonable to expect an average CN of 10.3 around P. This number agrees well with the RMC results of CN ≈ 10.6 for P in the $Ni_{80}P_{20}$ MG.[79]

The most frequent coordination polyhedron type around P is found to be ⟨0, 2, 8, 0⟩, which corresponds to the Kasper polyhedron with CN = 10. Kasper polyhedra[10,16,81,82] refer to ordered polyhedra with high symmetry whose surfaces are triangulated and usually involve a minimum number of declinations. In the case of Ni-P, our results are consistent with the previous finding[16] that the dominant polyhedron type is indeed bicapped square antiprism (BSAP) with Voronoi index ⟨0, 2, 8, 0⟩. The other two frequent types, namely ⟨0, 3, 6, 1⟩ and ⟨0, 2, 8, 1⟩, are considered as distorted BSAP. A systematic discussion on the two variants will be presented in "Nonuniform Particle Distribution

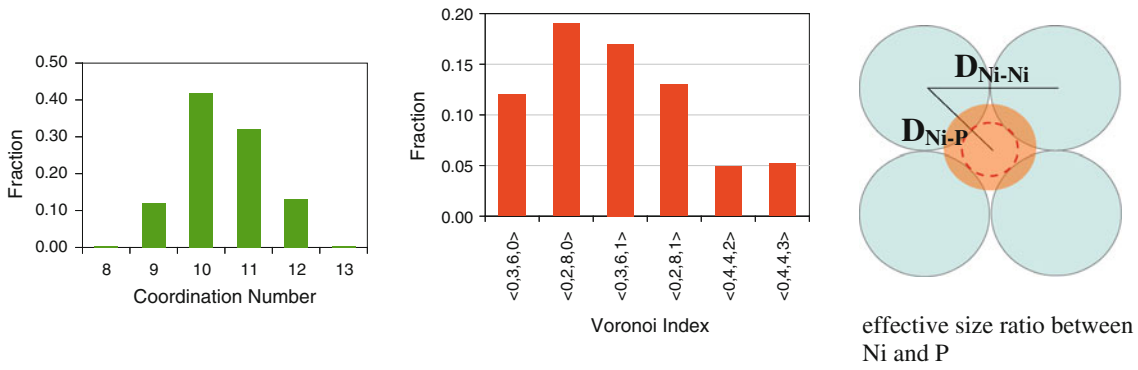

Fig. 4. (a) CN of P in the $Ni_{80}P_{20}$ MG at 300 K; (b) Voronoi index of the P-centered polyhedra. The dominant polyhedron type corresponds to bicapped square antiprism ⟨0, 2, 8, 0⟩. Only the polyhedra whose frequency is greater than 5% are shown. (c) Schematic showing how the effective size ratio between the solvent atom and the solute atom is determined. $D_{Ni\text{-}Ni}$ and $D_{Ni\text{-}P}$ refer to Ni-Ni and Ni-P bond distances.

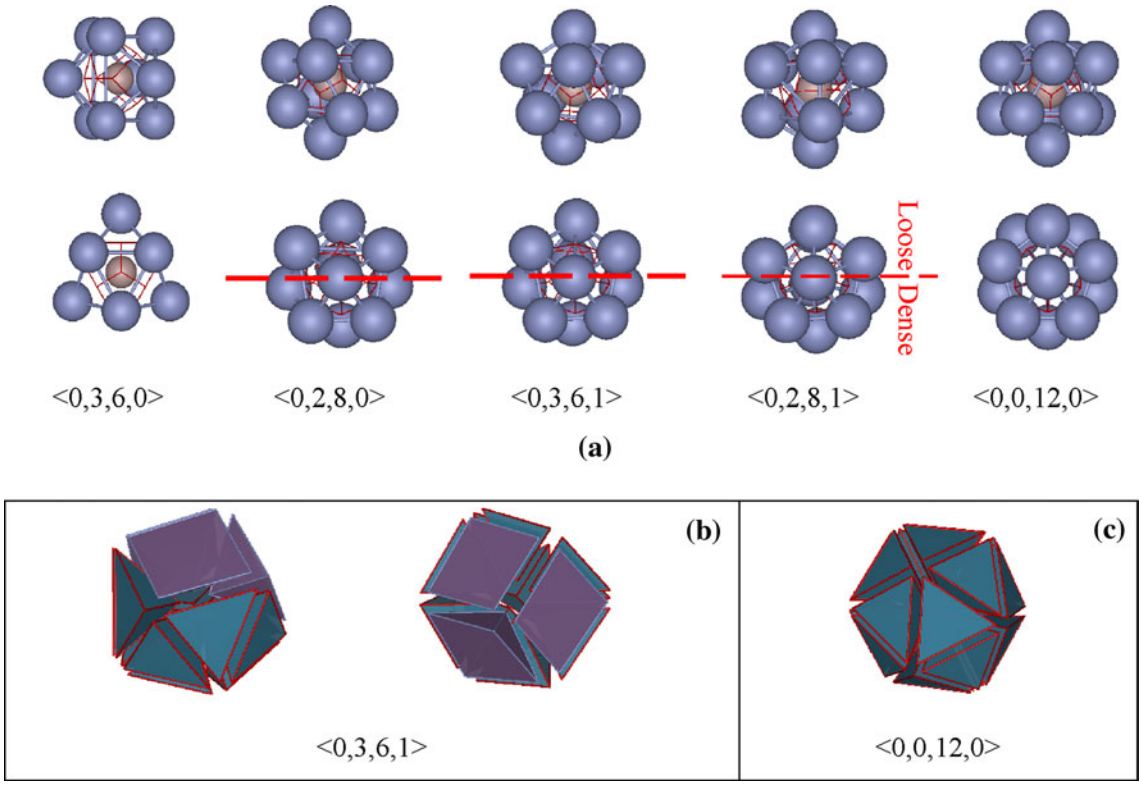

Fig. 5. (a) Atomic configurations for different types of polyhedra identified in the Ni-P MG. The dashed lines separate the polyhedra into loose packing and dense packing regions within the coordination shell. The nonuniform particle distribution is characteristic of ⟨0, 3, 6, 1⟩ and ⟨0, 2, 8, 1⟩ polyhedra. (b) ⟨0, 3, 6, 1⟩ polyhedra can be considered as packing of ten tetrahedra and three half-octahedra. The loose packing side is mainly due to the formation of half-octahedra. (c) A perfect icosahedron consisting of 20 equal-sized tetrahedra.

Within the Clusters" section to explain why the distorted polyhedra are important in this MG.

The total sum of the BSAP Kasper polyhedra and their variations reach as high as 50% of the total number of polyhedra. The majority of the remaining clusters are low-frequency irregular-shaped clusters. Therefore, the SRO of the Ni-P MG can be characterized as the BSAP type, which is distinctly different from the ISRO common to many glass formers. It should be noted that the stereochemical compound Ni_3P ($I\bar{4}$)[88] has BSAP as its fundamental building block, as depicted in Fig. 5a. The development of the nonicosahedral SRO in the Ni-P MG is a progressive process, as shall be revealed below.

Structural Ordering and Potential Energy Landscape

To understand the formation of locally preferred clusters during the glass formation, we take the energy landscape view, which was originally proposed by Goldstein[89] and later formulated by a number of researchers.[46,61,90,91] In this view, liquid kinetics and thermodynamics are dictated by the energy landscape, or the potential energy surface (PES), of the system. During the cooling process, liquids gradually sample deeper energy basins on the PES, characterized by potential energy minima and the energy barriers that separate the energy basins, as schematically shown in Fig. 6. The structures corresponding to the energy minima are termed inherent structures (IS). In the following we report the structural aspect of the PES during the glass formation, through the studies of the IS of the

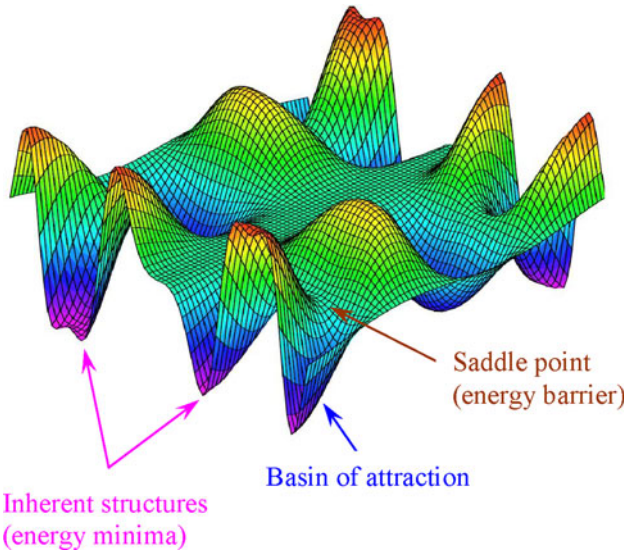

Fig. 6. A schematic drawing illustrating some important locations on an energy landscape.

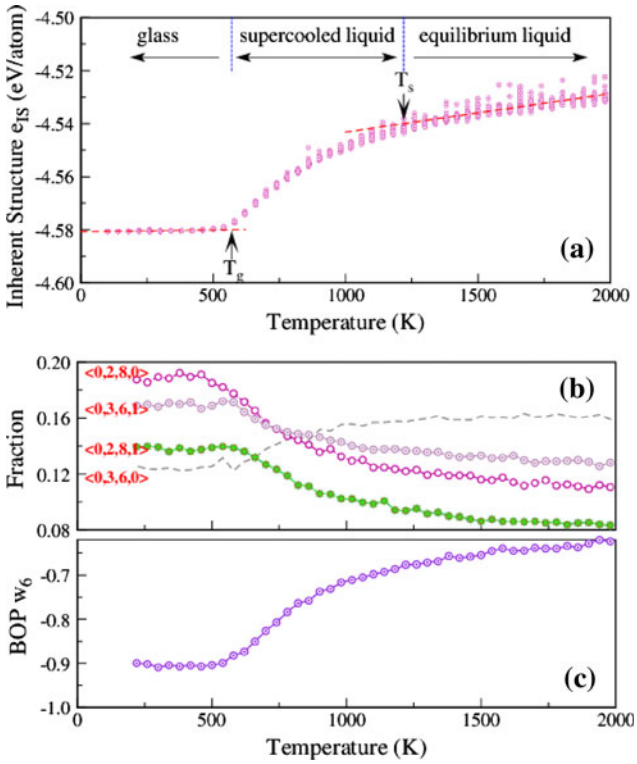

Fig. 7. (a) IS energy as a function of temperature. T_s denotes the onset dynamic slowing-down temperature. The dashed lines are only a guide to the eye. (b) SRO during the glass formation. The Voronoi tessellation analysis was conducted on the IS at different temperatures to remove the thermal effect. The rapid rise of the ⟨0, 2, 8, 0⟩ during the glass transition indicates that the SRO belongs to the BSAP type. (c) Shape-spectroscopy order parameter w_6 (x100) as a function of temperature, showing the topological ordering of local clusters during the glass transition.

system. In this way, we are able to separate the thermal contribution from the intrinsic configurational contribution to structural ordering.

We demonstrate the potential energies of the IS of the liquid at different temperatures during the cooling of Ni-P. IS can be obtained by quenching high-temperature configurations with an infinitely high cooling rate. Different from previous research that mainly focused on the constant-volume behavior,[61] for practical reasons, we studied the constant-pressure behavior of the Ni-P glass. To reach the constant-pressure condition, the volume of the system was relaxed simultaneously during the geometric minimization of atom positions, such that the internal pressure of the IS was always equal to ambient pressure. Figure 7 shows the potential energies of the IS of the liquid during the cooling of Ni-P under the constant-pressure condition.

The general features of constant-pressure IS are similar to those of the constant-volume condition.[61] During the glass formation, deeper basins with lower IS energies are explored as the temperature is lowered. Three regimes of the IS can be identified, marked by two crossover temperatures. The three regimes are closely related to the dynamics of the liquid. Above the dynamic crossover temperature, T_s, liquids freely sample the PES. Below the dynamic crossover temperature, the liquid enters its supercooled region and the liquid dynamics is influenced by the energy barriers of the PES. The IS energy decreases with an accelerated rate, then hits a plateau indicating that the liquid samples limited configurational space when the temperature is below the glass-transition temperature.

The change of the IS energy is closely correlated with the structural ordering of IS, as reflected by topological analysis of the local clusters. It was found that the frequency of locally preferred clusters gradually increases with decreasing temperature, in a similar fashion as the IS. For high-temperature equilibrium liquids, the percentages of the BSAP-related clusters of the IS remain relatively low. Structural ordering becomes pronounced when the system is supercooled below T_s, and finally becomes stabilized below the glass-transition temperature. It is noteworthy that the structural ordering of the ⟨0, 2, 8, 0⟩-type polyhedron rises more rapidly than that of the other major polyhedron types (⟨0, 3, 6, 1⟩ and ⟨0, 2, 8, 1⟩), supporting the idea that the BSAP-type Kasper polyhedra are indeed the favored clusters.

Structural ordering of local clusters was further confirmed by bond-orientational order parameter (BOP) analysis.[92] The BOP is derived from the spherical harmonics associated with atomic bonds[92] and contains rich information about the "shape spectroscopy" of the liquids and glasses. As opposed to the local BOP q_6 commonly used for ISRO, we find that, among all the BOP parameters, the w_6 shape parameter is most effective to characterize the BSAP–SRO. The w_6 parameter was calculated for each coordination polyhedron around P and then averaged over all solute atoms in the ensemble. The w_6 values are presented in Fig. 7b. The trend of w_6 is consistent with that of the Voronoi index and IS energy. Quantitative differences of the SRO exist between low-temperature IS and high-temperature IS. The IS for high-temperature liquids can be considered as "unrelaxed" glasses (quenched with an infinitely high cooling rate as a limiting case). In this work, we systematically study the IS at 1980 K (denoted as IS_L) and the IS at 300 K (denoted as IS_G) to represent two types of glasses with contrasting degrees of structural ordering, such that the role of structural ordering in dynamic properties can be better illustrated.

Nonuniform Particle Distribution Within the Clusters

In addition to the dominant BSAP type, there are a sizeable proportion of other types of competing polyhedra. It is essential to dissect the relationship between ordered BSAP and other types of polyhedra in the glass.

Perfect BSAPs (⟨0, 2, 8, 0⟩) have two fourfold bonds and D_{4d} symmetry. A schematic drawing is

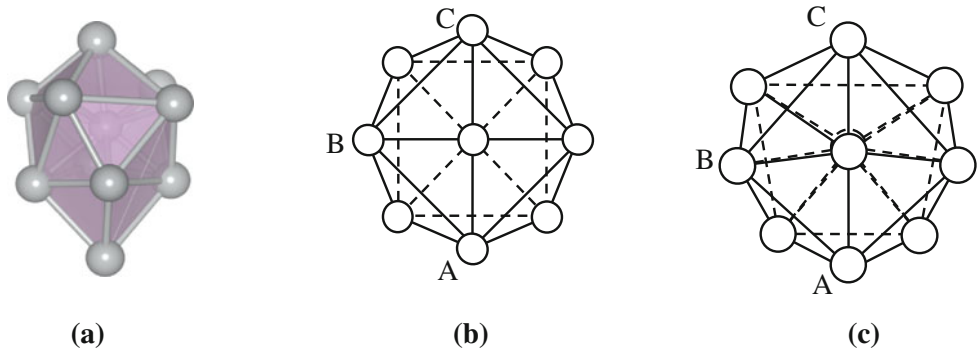

Fig. 8. (a) Atomic configuration of a BSAP identified in the Ni_3P ($I\bar{4}$) compound, with the Voronoi index ⟨0, 2, 8, 0⟩. Note that not all the Ni-Ni bond distances are equal in the Ni_3P compound. (b) A perfect BSAP has D4d symmetry. (c) Schematic showing the bond-relaxed BSAP configuration. Nonuniform particle distribution is obvious in the distorted polyhedron, which still has the ⟨0, 2, 8, 0⟩ Voronoi index.

provided in Fig. 8b to show the atomic arrangement of a BSAP viewed from above. Bond stretching is necessary to maintain the high symmetry of perfect ⟨0, 2, 8, 0⟩, as illustrated by the A–B and B–C bonds shown in Fig. 8b. In other words, high-symmetry BSAPs can only be formed by packing 16 bond-stretched tetrahedra. Without additional geometric or energetic constraints in the short to medium range to stabilize the stretched bonds, ⟨0, 2, 8, 0⟩ polyhedra always have a tendency to rearrange themselves to minimize the number of stretched bonds and to maximize the number of regular tetrahedra, resulting in distorted ⟨0, 2, 8, 0⟩ polyhedra (Fig. 8c). The rearrangement invariably reduces the symmetry of the cluster, leading to nonuniform particle distribution around the center atom. On one side of the cluster, more "regular" (3 Ni atoms + 1 P atom) tetrahedra with relaxed bonds appear, causing dense packing of atoms on this side. By contrast, the other side of the cluster is deficient of atoms, and the packing features more distorted tetrahedra. If the nonuniformity is further increased (e.g., atom C in Fig. 6c shifts to the left), the Voronoi index changes from ⟨0, 2, 8, 0⟩ to ⟨0, 3, 6, 1⟩. The ⟨0, 3, 6, 1⟩ type is a typical example showing nonuniform atomic packing in the first coordination shell, which can be formed by packing ten "regular" tetrahedra (three Ni atoms and one P atom) and three half-octahedra. Consequently, large unoccupied volume opens up in the atomic environment. The ⟨0, 2, 8, 1⟩ type is a variation of ⟨0, 3, 6, 1⟩, with an additional atom packed into the loose region. Atomic configurations showing the nonuniform atomic packing for ⟨0, 2, 8, 0⟩, ⟨0, 3, 6, 1⟩, and ⟨0, 2, 8, 1⟩ are presented in Fig. 5. The ⟨0, 2, 8, 1⟩ polyhedron can also be considered as a distorted icosahedron with one atom missing from the icosahedral packing.

Common to distorted ⟨0, 2, 8, 0⟩, ⟨0, 3, 6, 1⟩, and ⟨0, 2, 8, 1⟩ polyhedra is that there exist densely packed (DP) and loosely packed (LP) halves in the coordination shell. On the dense-packing side, atoms are more efficiently packed, typically featuring fivefold atomic bonds. The formation of fivefold bonds enhances the stability of the clusters, which explains why they are among the favored clusters. On the loose-packing side, atoms are highly prone to external perturbation, thermally or mechanically, due to too much "elbow" room available to accommodate their movement. Of course, for other irregular-shaped polyhedra with more nontriangulated faces, the nonuniform particle distribution feature is even more pronounced.

Loose packing in the first coordination shell seems to be the norm for clusters with CN around 10 or 11, and they are intrinsically inefficient packing clusters. This scenario does not hold true for icosahedral SRO packing or TTP SRO packing. It is thus conceivable that the atomic packing efficiency in CN = 10 or CN = 11 glasses (featuring BSAP–SRO) is less than that of icosahedral SRO, which may explain why excellent binary glass formers tend to have either icosahedral or TTP type of SRO.

The nonuniform particle distribution in the first atomic shell will contribute greatly to the formation of subatomic voids, leading to the phenomenon of "first-coordination-shell particle deficiency" as discussed in "Particle Deficiency in the First Coordination Shell of LP Atoms" section. Experimentally, the lack of site symmetry in MGs can be detected with SRO-sensitive probes, such as nuclear magnetic resonance (NMR). A recent study[28] employing NMR showed that some solute atoms in MGs may lack site symmetry, as demonstrated by Al in the Ce-Al-Cu MG. Microalloying the sample with Co increases the geometric site symmetry of Al and also enhances the glass-forming ability of the system.[28]

Medium-Range Structural Ordering

Despite the differences in the fine detail of atomic packing, the solute-centered clusters can still be regarded as "quasi-equivalent," due to the fact that they have similar CN and comparable polyhedron volumes. These clusters connect with each other and form extended structures in the medium range. To shed light on the packing scheme of the clusters, we conducted common neighbor analyses (CNA)[93] on the clusters. In the CNA method, each cluster is

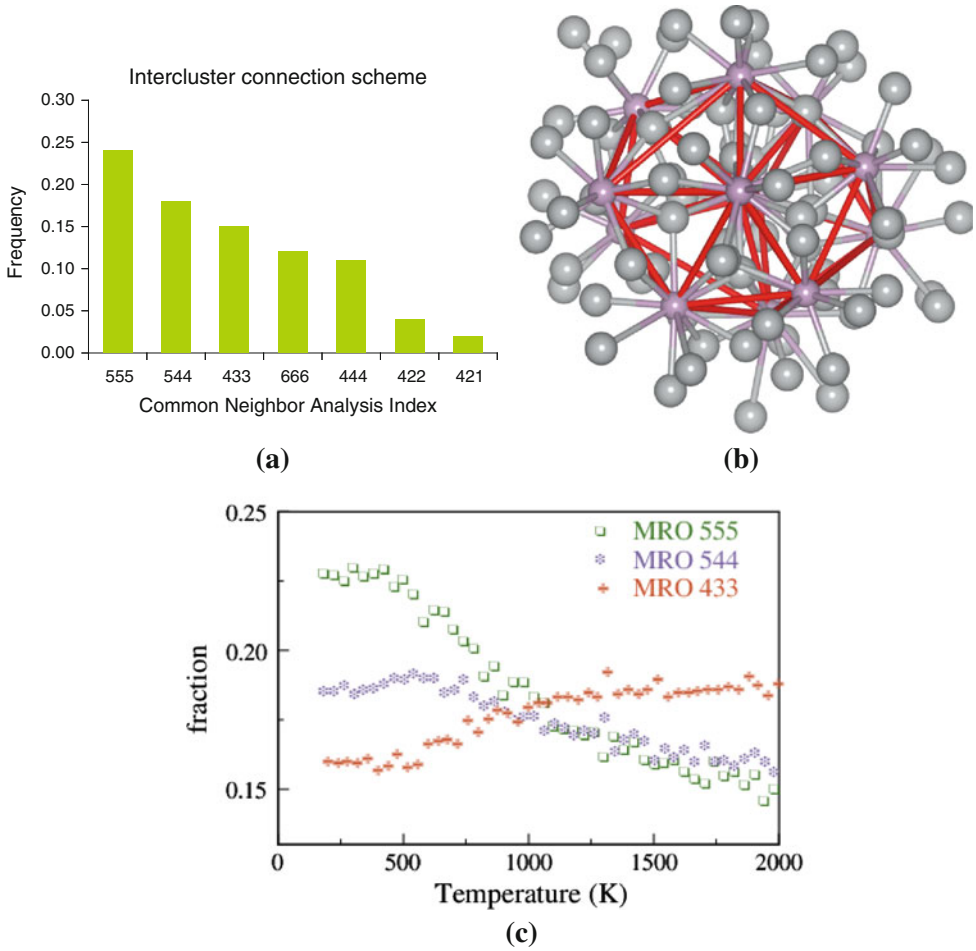

Fig. 9. (a) CNA index of the cluster packing in the Ni-P metallic glass, where fivefold cluster packing is dominant. (b) A perfect icosahedron formed with 12 quasi-equivalent clusters. The red lines denote the "bonds" between two neighboring clusters. All the intercluster connections have fivefold symmetry. (c) Medium-range ordering as a function of temperature during the glass formation. The analysis was conducted on the IS at different temperatures (Color figure online).

treated as an entity. If the centers of two clusters are within a cutoff distance (6.0 Å in this work), they are considered as nearest neighbors. The CNA analysis produces a set of *jkl* triplets, where *j* is the number of nearest neighbors common to both clusters, *k* is the number of cluster connections among the *j* clusters, and *l* is the number of cluster connections in the longest continuous chain formed by the *k* connections. The CNA may shed light on the cluster environment; For instance, a CNA index of 555 indicates fivefold cluster packing. The results of the CNA analysis are provided in Fig. 9a. The total sum of fivefold bonding (555) and quasi-fivefold bonding (544) reaches around 45%, indicating that clusters tend to pack themselves very densely in the medium range. The dominance of fivefold intercluster connection suggests that cluster packing in the medium range involve complex non-space-tiling schemes that simple face-centered cubic (fcc)- or body-centered cubic (bcc)-like medium-range ordering (MRO) cannot describe. In the Ni-P glass, we actually detected large icosahedra consisting of 12 P-centered clusters via vertex, edge, and face sharing, as shown in Fig. 9b. The MRO identified here is in quantitative agreement with what we reported in Ref. 16. One should be cautioned that the appearance of fivefold cluster connection does not always mean perfect icosahedral cluster packing.

The evolution of atomic packing in the medium range, i.e., medium-range structural ordering, during the cooling process was analyzed by conducting CNA analysis on the IS at different temperatures. The major CNA indices of the intercluster connection are plotted in Fig. 9c as a function of temperature. It is clear that the percentage of fivefold cluster connections increases with decreasing temperature, suggesting aggregation of the clusters during glass formation. The medium-range ordering is important, because it is related to the growing static correlation length[94,95] in the supercooled liquid. We believe that short-range structural ordering and medium-range structural ordering are concurrent processes that are mutually dependent during glass formation. More information on the MRO warrants in-depth investigations, and the results will be reported elsewhere.

SUBATOMIC VOIDS AS STRUCTURE DEFECTS IN METALLIC GLASSES

Substantial "voids" or cavities exist as a result of short- to medium-range cluster packing, especially the packing of "imperfect" clusters. In crystals, interstitial spaces (subatomic-sized "voids") are uniformly distributed in the lattice in the form of tetrahedral and octahedral sites. Without lattice constraints, voids in amorphous solids distribute differently. The distribution of voids in amorphous solids depends on the atomic packing of the system. Statistical information on large voids will not only enhance our understanding of structural ordering, but also serve as an important quantity to reveal hidden features of MGs. In his early work on hard-sphere packing,[96] Bernal characterized the geometry of five universal types of voids, termed as "Bernal's canonical holes." Later on, much work demonstrated that the types of holes in liquids or glasses appear to be too large for convenient classcification.[97–99] In what follows, we conduct systematic investigation on the geometry of voids in this MG, and reveal important properties associated with the structural defects.

Subatomic Voids in Metallic Glasses

To quantify the voids or cavities within MGs, two complementary methods are used. The first method involves use of the electron charge density distribution,[16] usually obtained from electronic calculations. The charge density can be used to delineate the void space by plotting charge density isosurfaces, with low-charge-density regions defining the void space in the structure. With this method, large cavities among solute-centered clusters were previously identified in the Ni-P MG generated by ab initio MD,[16] as shown in Fig. 10a. A similar approach based on linear superpositions of atomic charge density (similar to the spirit of the Harris functional[100]) was developed by Bharathula et al.[101] to quantify the open-volume distribution in a Cu-Zr MG.

Alternatively, statistical geometry anaysis[99,102,103] can be performed on prebuilt MG configurations to extract void information, based on spatial tessellation and exclusion of volumes occupied by the atoms. In this work, we use Sastry's algorithm to identify large voids, which actually correspond to void configurations with a number of atoms enclosing the voids. A schematic is provided to show how voids can be mathematically located using the algorithm proposed by Sastry et al.[102] Having obtained the voids, for visualization purposes, we sometimes subject large clusters (carved from the MG configurations) containing the voids to ab initio calculations and derive their charge density distribution to delineate the void spaces.

In Sastry's method, the only important parameter is the exclusion radius for each species, as indicated by the yellow spheres in the schematic drawing in Fig. 10c. We set the exclusion radii to be 1.45 times the atomic radii of Ni (1.25 Å) and P (1.10 Å), respectively, which are slightly larger than the Bernal length (approximately 1.4 times the radius).[96] The exclusion radii are selected such that they are large enough to exclude ordinary tetrahedral sites and octahedral sites from the void enumeration. These exclusion radii would produce a comparable amount of LP atoms (i.e., atoms adjacent to the voids) and DP atoms in the glass, as shown in the next section. Of course, if one is to find larger voids in the glass, the exclusion radii can always be enlarged.

Large voids found in the IS_G glass are enclosed by a number of atoms (ranging from 4 to as many as 12 atoms). Typical void configurations are presented in Fig. 10d. It is immediately obvious that the voids always involve P atoms and exist as a result of cluster packing. The radial size of the voids can be roughly determined by inserting a sphere into the void space without perturbing the surrounding atoms. With the exclusion radii we used, the radius of the *smallest* void is estimated to be around 0.6 Å, which is larger than the size of octahedral holes in close-packing atomic arrangements in crystals. For large voids, their volumes are much bigger but usually with complex shapes (see the next section). If approximated as hard-sphere packing, the largest sphere that can be inserted into the holes has radius around 1.05 Å, which is comparable to the size of small atoms (such as P). It is thus justifiable to call those voids "subatomic" voids. Atoms that enclose the voids are called LP atoms, and those that are not associated with the voids are called DP atoms.

We compared the number of large voids found in the 32,000-atom configurations for both unrelaxed IS_L and relaxed IS_G glasses. The results are shown in Fig. 11a. For the unrelaxed glass IS_L, both the total number of voids and the number of "large voids" (involving as many as 20–30 atoms) are significantly greater than those of relaxed glass IS_G, pointing to the facts that (1) more atoms are LP in the liquid inherent structure IS_G, and (2) with increasing structural ordering, large voids are broken down and many voids are annihilated due to the formation of ordered polyhedra. Annihilation of voids is thus a manifestation of short- to medium-range structural ordering. The result can be further confirmed by the reduction of LP atoms during the relaxation process. Figure 12b shows the percentage of void-adjacent atoms (i.e., LP atoms) of the IS at different temperatures. During glass formation, large spread-out voids are squeezed out, delocalized, and redistributed among different clusters during structural relaxation, leading to the reduction of the excess volume of the system (Fig. 12a).

In amorphous solids, it is informative to investigate the geometric shapes of the voids. To this end, we characterized the asphericity parameter, R,[104] of each void. The asphericity parameter was derived from the gyration tensor S of the void configuration. Diagonalizing the gyration tensor S, we obtain three

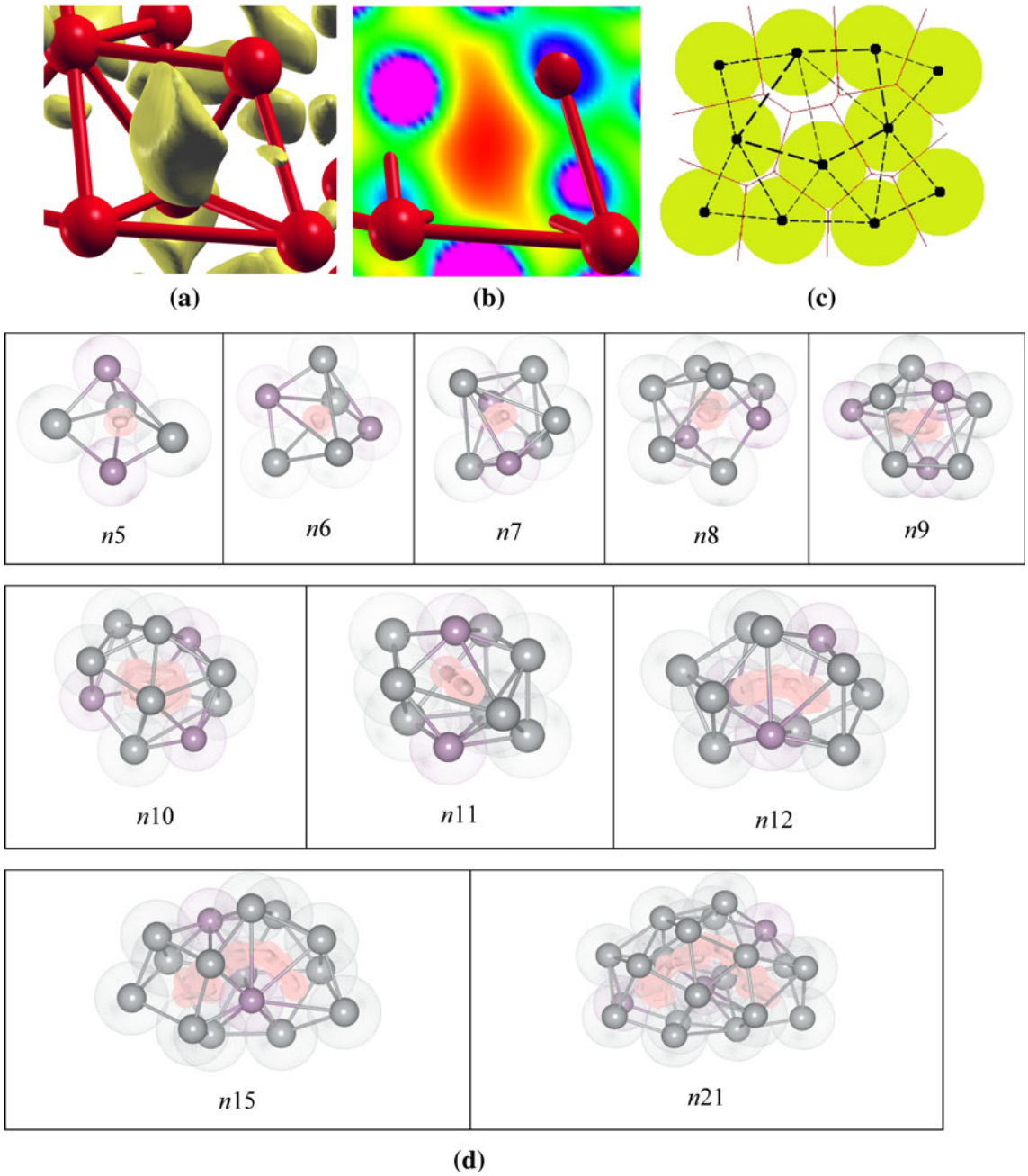

Fig. 10. (a) Large cavities identified in a $Ni_{80}P_{20}$ MG generated with ab initio MD.[16] The cavities correspond to low-charge-density zones. (b) A cut plane showing the charge density distribution. (c) Sastry's method[102] to locate large voids in the glass configuration. Two-dimensional (2D) schematic of exclusion discs is shown with its corresponding Voronoi (red lines) and Delaunay (dashed lines) tessellations. A set of Voronoi vertices connected by edges that lie entirely within the void region represents a cavity. (d) Typical void configurations found in the IS_G glass. Gray spheres represent Ni, and pink spheres represent P. The void spaces enclosed by the atoms are schematically represented by thick bonds connecting the Voronoi vertices. As the voids grow larger, the shape of the voids tends to be cylindrical (see n12–n21) (Color figure online).

principal moments $\lambda_x^2 < \lambda_y^2 < \lambda_z^2$. The asphericity parameter R is defined as

$$\frac{\lambda_z^2 - (\lambda_x^2 + \lambda_y^2)/2}{\lambda_x^2 + \lambda_y^2 + \lambda_z^2},$$

where $R = 0$ corresponds to the perfect spherical shape, and large R refers to high asphericity of the shape. It is found that, with increasing number of atoms involved in the void, the shape deviates more from the spherical shape. This result is qualitatively consistent with visual inspection of Fig. 11d, where the shape of large voids becomes highly nonspherical and has a tendency to form cylindrical or tubular structure (see, e.g., the *n12*, *n15*, and *n21* void configurations in Fig. 11d). However, for further large voids ($n > 20$), the asphericity parameter does not seem to increase accordingly. In fact we found

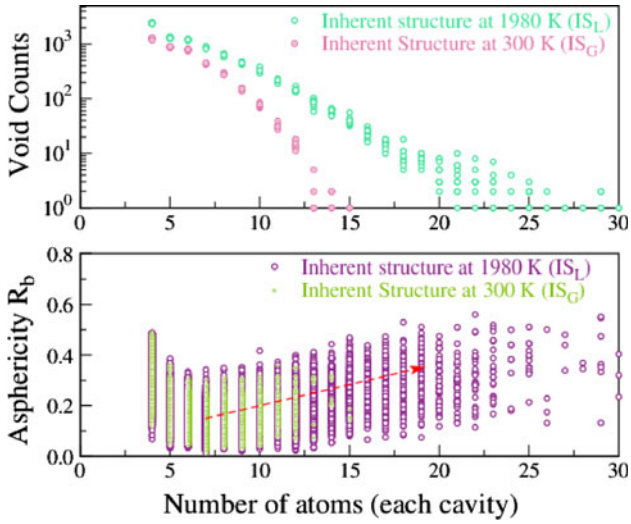

Fig. 11. Top panel: void statistics for the IS_G and IS_L configurations. Bottom panel: asphericity parameters for the voids identified in the two structures. As the voids grow larger, the asphericity parameter also increases, indicating that the shapes become increasingly nonspherical. The large voids in the IS_L configuration involve more atoms, and form complex shapes.

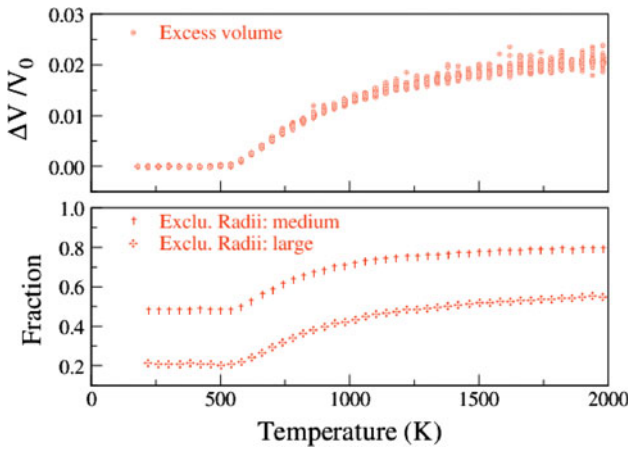

Fig. 12. Top panel: excess volume of the IS at different temperatures, which was normalized against the volume of the IS_G configuration V_0. For the unrelaxed IS_L, the excess volume reaches as large as 2.5%. Bottom panel: the number of atoms adjacent to voids (defined as LP atoms) in the IS at different temperatures. Large exclusion radii correspond to large voids found in the structure.

that the shapes of the large voids tend to be "disc"-like. Because of their complex shapes, these voids may appear to be subnanometer sized for some experimental probes, such as the positron annihilation technique.[105] The shapes of the voids have implications for the atomic transport mechanisms of MGs (see "Atomic Diffusion Mechanisms and Structural Defects" section).

Spatial Distribution of Voids and Structural Inhomogeneity

The spatial distribution of the voids was examined by their RDF, where the voids were treated as a hypothetical massless component of the glass. The center positions of the voids were taken from the Voronoi vertices located in the void region (Fig. 10b; see Ref. 102 for details). The void–void, void–Ni, and void–P RDFs are shown in Fig. 13 for the relaxed MG IS_G. For the void–void distribution, the first meaningful peak appears to be at 3.30 Å (convolution of two subpeaks), indicating that the *average* void–void interaction is only separated by one or two atomic layers. For the void–P and void–Ni pair correlations, as expected, the first peaks correspond to the exclusion radii of P and Ni. An extended tail is found to follow the main peaks of the void–P RDF. The position of the shoulder coincides with the position of the first peak of the Ni-P RDF in Fig. 2. The physical meaning of this phenomenon is that, in the first coordination shell of P, there exists a finite probability of finding large voids. This confirms our finding in "Nonuniform Particle Distribution Within the Clusters" section that atoms around P may be unevenly distributed, contributing to the formation of voids.

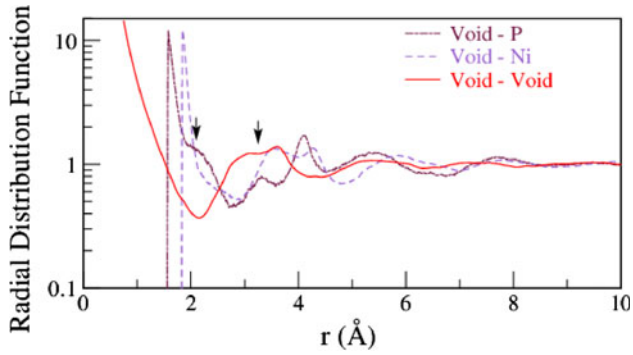

Fig. 13. RDF of different species around voids.

The voids are not homogeneously distributed in the glass. Figure 14a shows the distribution of DP atoms (not adjacent to voids) in the IS_G glass within a thickness of 5.5 Å. Patches of connected DP atoms are visible, indicating that these regions are DP with high atomic packing density. On the other hand, voids agglomerate in the loose-packing regions and seem to have a correlation length of about 1–2 nm (Fig. 14a). The atomic number density in these regions is relatively low, which renders the glassy structure rather inhomogeneous. The local density fluctuation reaches as large as 5% based on the volume data presented in the next section. Such a structural feature has been suggested previously by a number of experimental techniques in MGs,[34,42,43] and here we show computational evidence to corroborate this hypothesis.

Figure 14 shows how the LP and DP regions grow with temperature during the cooling process. At high temperatures (e.g., 1980 K), a few DP clusters appear in the IS, and they gradually increase in number with decreasing temperature. In the supercooled liquid, the DP clusters show obvious spatial heterogeneity, having fractal-like morphologies, as

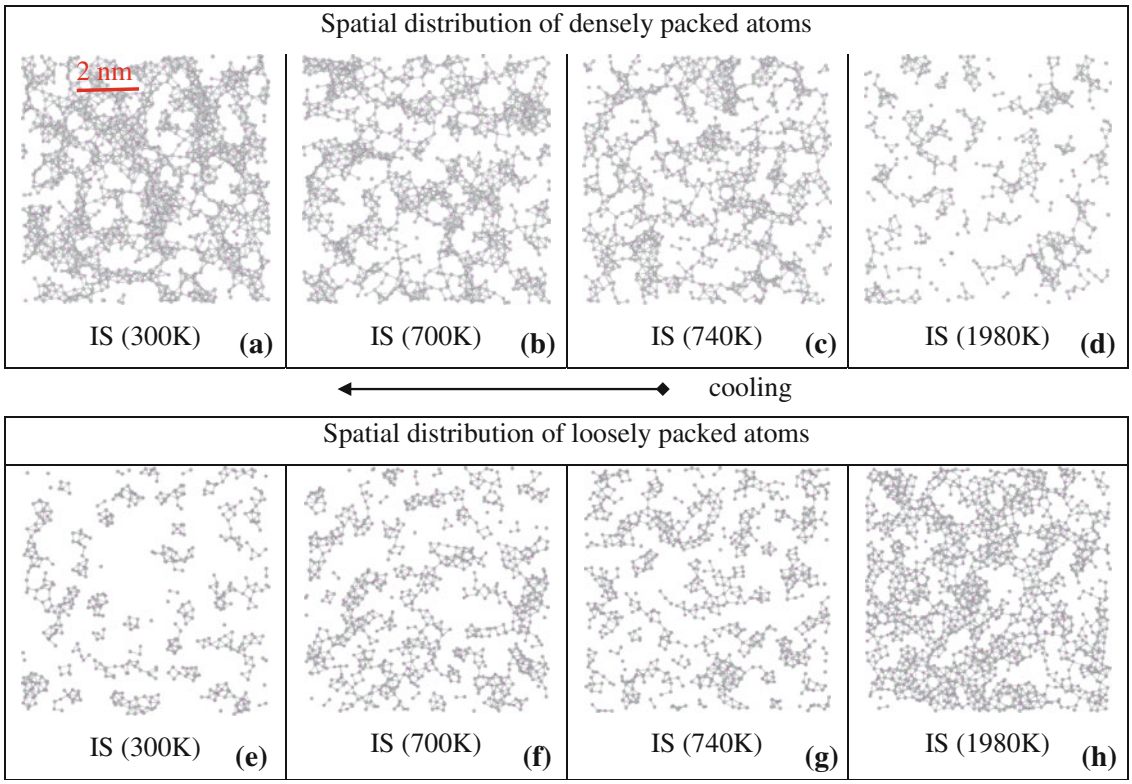

Fig. 14. Top: spatial connection of DP atoms in the IS at different temperatures during the cooling process, to illustrate spatial heterogeneity. Atomic number density is high in the DP regions. Bottom: spatial connection of LP atoms of the IS at different temperatures.

shown in Fig. 14b–d. On the contrary, the number of LP clusters gradually decreases, but they remain spatially inhomogeneous (Fig. 14e–h). It would be interesting to explore the correlations between spatial heterogeneity (in terms of void distribution) and dynamic heterogeneity of the supercooled liquid, which, however, is beyond the scope of this article.

Properties of Voids and LP Atoms

As demonstrated above, atoms in MGs can be separated into two classes based on their connectivity with the voids: those that are associated with the voids versus those that are not, i.e., DP atoms and LP atoms. This classification is based on the fact that the two classes of atoms have very different properties in terms of atomic volume, CN, energy, SRO, coordination polyhedron anisotropy (site symmetry), etc. Figures 15 and 16 systematically compare the properties of the LP and DP atoms in the IS_G glass.

Figure 15a and b shows the atomic volume distribution of the LP and DP atoms for Ni and P, respectively. In both cases, LP atoms have larger atomic volumes than DP atoms, and the average difference is about 5%, indicating that LP atoms have much larger volume than DP atoms. Our atomic-level stresses analysis demonstrates that LP atoms have larger volume strain than DP atoms (not shown here).

Figure 15c and d shows the potential energy distribution of the LP and DP atoms for Ni and P, respectively. The potential energy for each atom was calculated from the EAM formalism. It is interesting to see that the energetics of the LP and DP atoms behave quantitatively differently for the species Ni and P. LP Ni atoms have higher potential energies than DP Ni atoms, whereas P atoms exhibit the reverse trend, implying that LP P atoms are more locally favorable. This seems to be counterintuitive because P atoms tend to be DP with more $\langle 0, 2, 8, 0\rangle$ polyhedra forming during structural relaxation/ordering. Further inspection reveals that structural ordering involves both the center atom and the atoms in the coordination shell. The potential energy of single atoms *cannot* be used as an indicator for structural stability. In the current case, the energy loss of the solute atoms due to structural ordering is compensated by the energy gain of surrounding Ni atoms through void annihilation. Collectively, there is a driving force for the structural ordering of BSAP polyhedron.

Figure 16a, b displays the CN distribution of the LP and DP atoms. The CN was calculated by counting the number of nearest atoms within a cutoff distance (2.9 Å for P and 3.1 Å for Ni). As expected, the LP atoms have smaller CNs than the DP atoms. The average CNs for LP P and DP P are 9.18 and 9.85, respectively. The average CNs for LP Ni and DP Ni are 12.23 and 12.70, respectively.

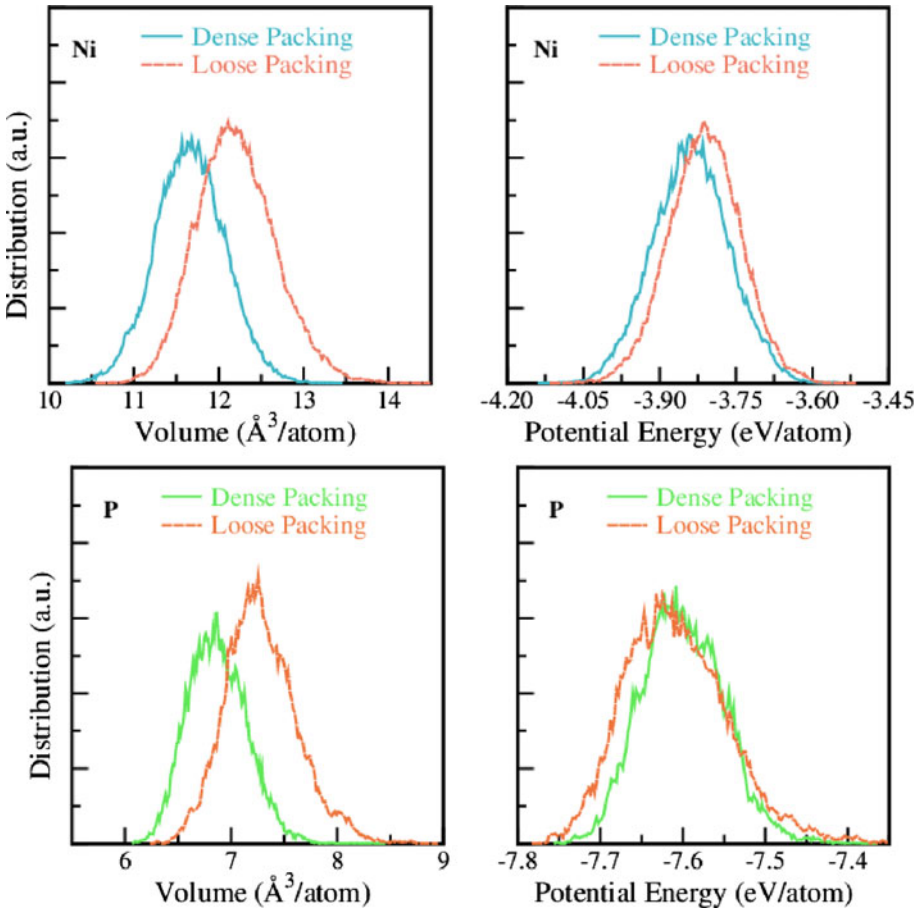

Fig. 15. Potential energy and volume distribution of LP atoms versus DP atoms in the Ni-P MG.

Such a CN difference is considered to be large, reflecting packing density differences of the two groups of atoms. In fact, this first-coordination-shell particle deficiency is further demonstrated in "Particle Deficiency in the First Coordination Shell of LP Atoms" section.

Figure 16c, d shows the atomic environment around both Ni atoms and P atoms. To better illustrate the differences of the atomic environment, we used the bond-orientational order q_6 for Ni, and used the Voronoi index for P atoms. It is obvious that most of the LP solute atoms have more irregular-shaped coordination polyhedra. A substantial amount of $\langle 0, 3, 6, 1\rangle$ and $\langle 0, 2, 8, 1\rangle$ polyhedra types are found in the LP atomic group. For the DP atoms, ordered Kasper polyhedra are the dominant type. Kasper polyhedra are usually considered as dense-packing polyhedra (being even truer in the case of ISRO). It is therefore justifiable to use Kasper polyhedra as an indicator for dense packing in MGs.[106–108]

Particle Deficiency in the First Coordination Shell of LP Atoms

One hidden feature of the LP atoms in MGs is that they exhibit the phenomenon of first-coordination-shell particle deficiency. To illustrate this, we plot the partial RDFs of the LP particles. The partial RDFs of LP atoms refer to the distribution probability of all atoms (both LP and DP atoms) around LP atoms. Figure 17 shows the comparison between LP atoms and DP atoms in the IS_G MG. Quantitative differences can be found between the two classes of atoms. Firstly, the intensity of the first peak for the LP atoms is lower than that for DP atoms, implying that, within a fixed cutoff, the CN for LP particles is less than that for DP, as confirmed in Fig. 16a, b. This can be explained by an increased number of distorted tetrahedra and/or half-octahedra (shown in Fig. 2) in the coordination shell of the LP atoms. Secondly, a subtle but non-negligible peak appears between the first peak and the second peak, indicating a shortened bond distance between the LP atom and the second shell. This is due to the appearance of nontriangulated surface on the coordination polyhedra, which will be capped by another atom in the next coordination shell at a reduced distance. The formation of the small peak (between the first peak and second peak) may be characteristic of nonicosahedral atomic packing. This feature is associated with the formation of large voids (or packing of imperfect polyhedra) and has important implications in

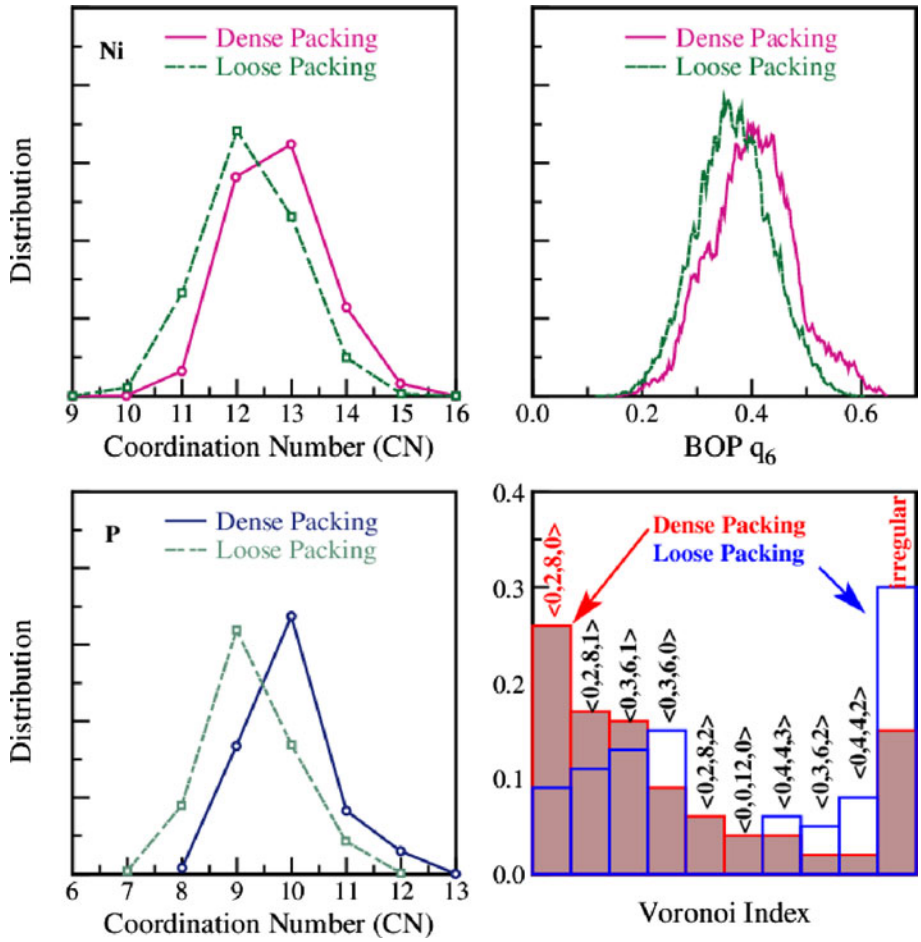

Fig. 16. Distribution of CN, BOP, and Voronoi index for LP atoms versus DP atoms.

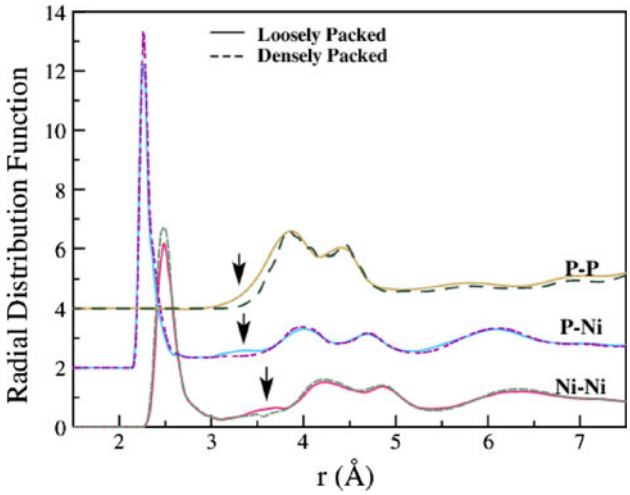

Fig. 17. RDF around the LP atoms and the DP atoms. The small peaks appearing around 3–4 Å are indicative of the formation of large voids. The intensity decrease of the first RDF peaks for the LP atoms indicates packing deficiency in the first coordination shell of LP atoms.

understanding the structural origin of quasilocalized vibrational modes as discussed in "Vibrational Properties and Structural Defects" section.

It is now fitting to compare the LP atoms with the "liquid-like" atoms in the free-volume treatment.[39] In the free-volume theory, atoms are characterized by their free volume (v_f), defined as the cell volume v minus the volume of the atom (v_0). If the free volume of the atom is greater than a critical value, the atom is called a liquid-like atom.

The subatomic voids discussed in this work are excess volumes concentrated among particles, which is essentially a topology-based defect due to packing deficiencies. As shown in Fig. 12, if the exclusion radii are set properly, LP atoms can be directly linked to liquid-like atoms, and DP atoms correspond to solid-like atoms, in terms of their quantity, Voronoi polyhedron volume, and spatial connectivity.

However, there are several differences between the void picture and the liquid-like atoms in the free-volume treatment: (1) Several LP atoms are connected around the same void. This collective feature cannot be captured by the free-volume treatment. (2) LP atoms are defined by their connection with voids, implying that the atoms are topologically distorted. Free volume on the other hand does not reflect the packing defects

(topological distortions of atoms). While the theory of atomic-level shear stresses was intended to account for topology distortions, its effectiveness for binary systems has yet to be demonstrated.[47–50] Therefore, the quantification of voids as structural defects in amorphous solids provides a microscopic picture to better understand the structure of glasses, and also serves as a useful vehicle to unravel the structure–property relationships of MGs.

VIBRATIONAL PROPERTIES AND STRUCTURAL DEFECTS

Vibrational properties of metallic glasses are fundamental perperties[109] that are directly connected to the thermodynamics and kinetics of MGs; For example, the normal mode vibrational density of states (VDOS) $g(\omega)$ affects barrier crossing rates on the potential energy landscape,[110] and enters Zwanzig's models[111] for self-diffusion of liquids and solids. Of course, vibrational properties are related to thermodynamic quantities as well as thermal properties such as thermal conductivity and specific heat.

A great puzzle about the vibrational properties of glasses is the appearance of the BP in $g(\omega)$. Debye theory predicts that at low frequency $g(\omega)$ is proportional to ω ($h\omega \sim 5$ meV). The BP is an excess peak at low vibrational frequency over that predicted by Debye theory in $g(\omega)$. This phenomenon has been observed by a number of experimental techniques such as inelastic scattering[112] and Raman spectroscopy,[113] and is considered a universal behavior for all glasses, although it appears that the intensity of the BP decreases with increasing fragility of the glass.[114] The physical origin of the BP has been controversial and has been considered a difficult problem in condensed matter physics. Theoretical work suggests that the BP arises from (quasi)localized and anharmonic vibrational modes associated with some defective structures.[115–120] The structural origin for the BP remains unsolved. In this work, we attempt to solve the structural origin of the BP by associating it with subatomic voids existing in MGs.

VDOS and Participation Ratio

The normal nodes of the glass can be obtained by diagonalizing the dynamical matrix of the IS, characterized by the eigenvectors and eigenfrequencies. We dealt with a smaller system (2048 atoms) for the vibrational properties of the $Ni_{80}P_{20}$ MG. The computational protocol for generating the 2048-atom MG is exactly the same as for the large sample used in the previous sections. The total VDOS was calculated from the eigenfrequencies using the expression

$$g(\omega) = \sum_j \Theta(\omega - \omega_j), \tag{6}$$

where Θ is a Gaussian smoothing function.

Experimentally, the VDOS for $Ni_{80}P_{20}$ metallic glass has been obtained through neutron scattering and is available in literature for comparison.[121] The experimental VDOS was expressed in the generalized vibrational density of states (GVDOS) form as[32]

$$G(\omega) = \sum_{i=1}^{m} W_i g_i(\omega) \Big/ \sum_{i=1}^{m} W_i, \tag{7}$$

where $G(\omega)$ is the GVDOS, m is the number of elements in the alloy, W_i is the effective weighting factor due to scattering cross-section, Debye–Waller factor, and atomic mass of element i, and $g_i(\omega)$ is the partial density of states (DOS). In our computation, the GVDOS was obtained by summing up the projected DOS (PDOS) of each element weighted with different factors. The PDOS is calculated from the normal mode eigenvectors and frequencies using the expression

$$g_i(\omega) = \sum_j \sum_{\tau}^{N_i} (e_\tau \cdot e^j)\Theta(\omega - \omega_j), \tag{8}$$

where e^j is the eigenvector for the jth normal mode with the corresponding frequency ω_j, N_j is the number of atoms of the ith element, and e_τ is the particular eigenvector component associated with individual atom τ. Taking the relative weighting factors ($W_i / \sum_{i=1}^{m} W_i$) of 0.68 and 0.32 for Ni and P, respectively, the configurationally averaged GVDOS of the $Ni_{80}P_{20}$ metallic glass is provided in Fig. 18. Also shown in Fig. 18 for comparison is the experimental GVDOS of melt-spun $Ni_{80}P_{20}$ MG. As expected, no van Hove singularities are seen in $g(\omega)$ for the amorphous sample. The agreement between the experimental and computational GVDOS is satisfactory. The two-band (with centers of gravity at 21 meV and 46 eV) structure of the spectrum has been well captured by the computation. The major contribution to the high-energy band comes from the solute atoms. Compared with the experiment, the simulated $g(\omega)$ is slightly broader. We investigated the $g(\omega)$ for several glasses produced with different cooling rates on the computer, and found that the cooling rate has an effect on the shape of $g(\omega)$ (not shown). The main peak (at ~21 meV) becomes slightly narrower if the cooling rate is slower. This implies that, if slower cooling rates are attainable in computation, a better match between computation and experiment can be achieved.

The experimental VDOS for polycrystalline Ni-P[121] with the same composition is shown for comparison with that of amorphous Ni-P. At low energies (below 10 meV), the $g(\omega)$ for crystalline Ni-P is found to be proportional to ω^2, following Debye theory. The excess BP is clearly visible for amorphous samples at this energy region. This feature becomes obvious if one plots $g(\omega)/\omega^2$ against ω, as shown in Fig. 18a.

A popular practice to interpret the BP is to analyze the atomic participation ratio of different

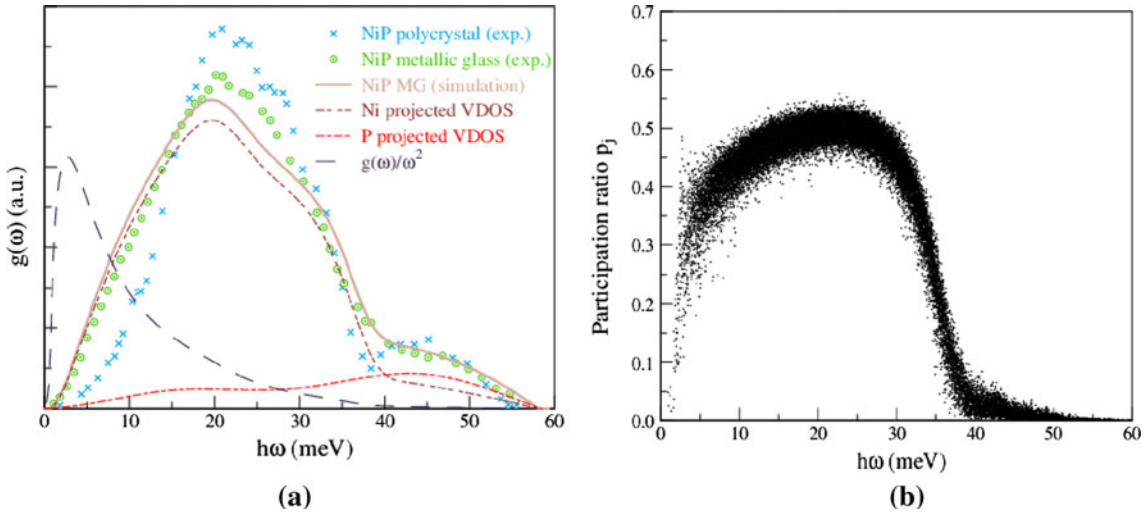

Fig. 18. (a) GVDOS of the IS_G glass. (b) Participation ratio versus frequency for the IS_G glass.

vibrational modes. For each mode, the participation ratio[115,117] can be calculated from the eigenvector

$$p_j = \frac{1}{N}\left[\sum_{i=1}^{N}(e_i \cdot e_i)^2\right]^{-1},$$

where e_i is the eigenvector associated with atom i for the jth vibration mode. For completely delocalized vibrational modes $p_j = 1$, and for modes localized to one atom (i.e., only one atom moves), $p_j = 1/N$. The participation ratio plot for the IS_G glass is shown in Fig. 18b. Several authors have found that vibrational modes are combinations of localized and extended modes.[115,117,120,122] Indeed, in the Ni-P MG, the vibrational modes in the central range have participation ratios around 0.5, consistent with previous findings. The vibrational modes are substantially localized at both ends of the vibration spectrum with small participation ratios.

At the high-energy end ($h\omega > 40$ meV), the participation ratio decays as $\sim 1/N$, indicating a reduced number of atoms involved in vibration in this energy range. These vibrational modes are truly localized. At the very high-energy end ($h\omega > 55$ meV), atomic vibration is localized on one to three atoms, primarily involving phosphorus atoms. We find that these modes can be well designated as cage-rattling modes of the solute atoms, reflecting the cluster arrangement of the glass. Such a feature seems to be common to TM–M MGs,[123–125] and the cage rattling of solute atoms should explain the high-energy band in $g(\omega)$ due to the strong interactions between resonating solute atoms and their caging solvent atoms.

Subatomic Voids as the Structural Origin for the BP

At the low-energy end ($h\omega < 10$ meV), approximately 1% of the vibrational modes have low participation ratios ($p_j < 0.25$). These modes are believed to be responsible for the BP in $g(\omega)$. Inspection of the lowest vibrational modes shows that those modes are not truly localized but rather involve a group of spatially correlated atoms. The number of atoms actively participating in the low-frequency vibration modes ranges from 20 to 200 atoms. (The criterion to select those atoms is based on their eigenvector amplitude $|e_\tau|$, and we count the number of atoms whose amplitude is greater than 20% of that of the most active atom). Nineteen atoms were found for the softest vibrational mode. Since the low-frequency modes are hybridized with acoustic modes, they are considered quasilocalized. Our results so far are in agreement with previous findings on MGs.[122,125,126]

The structural aspect of the low-frequency vibration modes have been explored extensively before. Laird and Schober[115] studied the RDFs of the actively participating atoms for several low eigenfrequencies. They found that the average CN of the actively participating atoms is less than the average glass environment and that a small but nonnegligible peak emerges between the first and second peak.[16] This bears a striking resemblance to what we reported for the voids, as shown in Fig. 17. The RDFs of the LP atoms adjacent to voids exhibit exactly the same feature, suggesting a close connection between voids and quasilocalized vibrational modes. We now set out to demonstrate that voids in MGs are indeed the structural origin for the quasilocalized modes.

Firstly, we examine how much contribution the LP and DP atoms respectively make to each vibration mode. For each eigenmode, we calculate their contribution coefficients $P(\omega)$ by projecting the eigenvectors onto the two sets of atoms

$$P(\omega) = \frac{1}{N_a}\left\langle \sum_{\tau}^{N_a} \left(e_\tau \cdot e^j\right)^2 \right\rangle,$$

where N_a is the number of atoms in each group and e_τ refers to the eigenvector coordinate of atom τ. If

the vibration modes do not have a structural origin, one would expect equal contributions from the two groups of atoms. Figure 19 displays the configuration- averaged contributions from the DP atoms and LP atoms. It can be seen that, at the low-energy end, LP atoms make a larger contribution to the vibration modes than the DP atoms. With increasing energy, the difference between the contributions from DP and LP atoms tends to diminish. It is worth noting that the vibration modes at the low-frequency regime comprise substantial contributions from sound waves. If the sound-wave-like part can be separated from the localized modes (see, e.g., Ref. 127), the contribution from the defect zones is expected to be more pronounced. At energies above the BP, the contributions from both the LP atoms and the tightly packed atoms become comparable, as expected from extended vibrational modes where atoms make equal contributions.

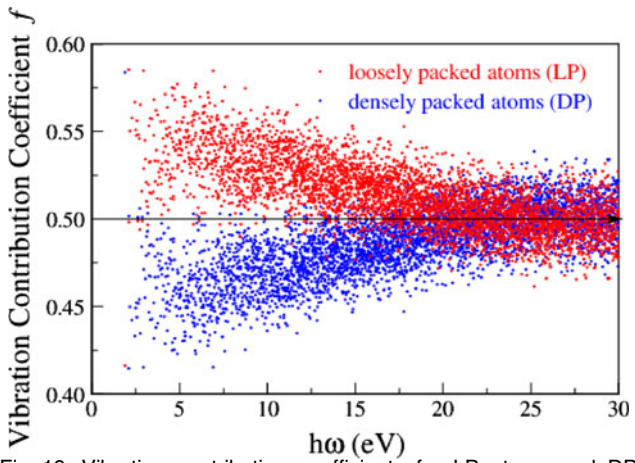

Fig. 19. Vibration contribution coefficients for LP atoms and DP atoms. At low frequency, LP atoms have a larger contribution coefficient than DP atoms, indicating that the vibration modes tend to be localized on LP atoms.

The close connection between subatomic voids and low-frequency modes can be further demonstrated by involving the eigenmode following technique.[117,119] In the simulations, the atoms are pushed away from the energy minima by following their eigenmodes until their restoring forces deviate significantly from the linear relationship. For the six softest modes, we push the atoms (whose displacements are greater than 20% of that of the most active atom,[119] termed "core atoms") from their minima to obtain their displacements as follows:

$$R^n(x) = R_0^n + xe^n, \tag{9}$$

where R_0^n is the equilibrium position of atom n, and e^n is the eigenvector component associated with the atom. Here, x represents the real displacement of the most active atom. Along the eigenmode path, the total potential energy $E(x)$ along the displacement path is shown in Fig. 20. The anharmonicity of the soft modes can be immediately identified from the shape of the potential function of the system, which can be best fitted with $E(x) = E_0 + Ax^2 + Bx^3 + Cx^4$, but not with a quadratic form.

The anharmonicity is mainly due to the particular atomic positions of the core atoms that participate in the vibration. To better understand the atomic environment of these atoms, the variation of the potential energy of the 19 actively participating atoms in the softest mode is plotted in Fig. 20. It is interesting to see that, for this group of atoms, their

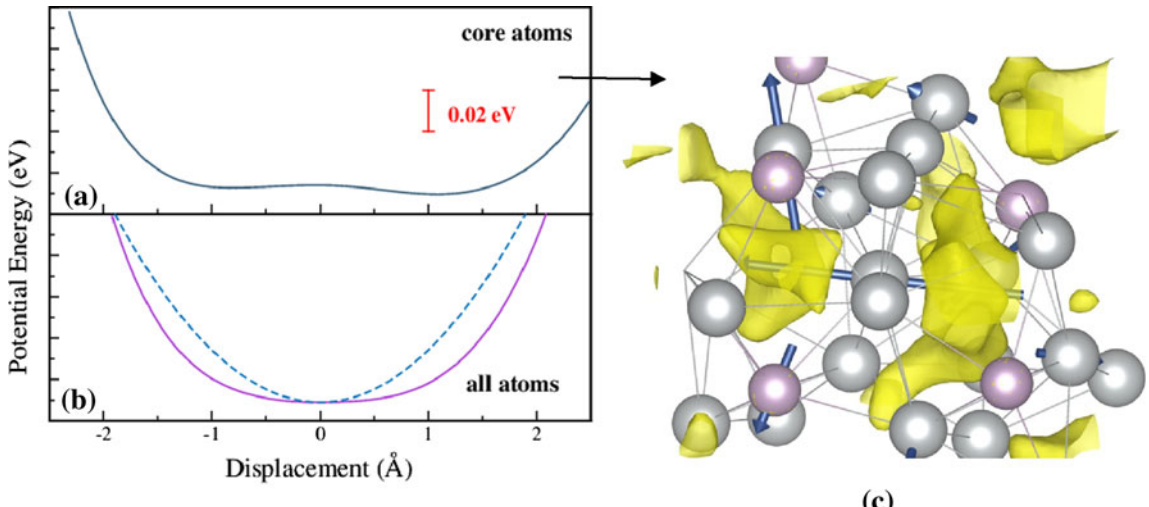

Fig. 20. (a) Average potential energy of atoms in the softest vibration mode ($h\omega$ = 1.35 meV). The core atoms include atoms whose amplitude is at least 20% of the maximal atomic amplitude in the mode. In the softest mode, 19 atoms were included in the calculation. The displacement refers to the displacement of the most active atom in the vibration mode. (b) Average potential of the entire system. The dashed line schematically shows what the potential energy looks like in a harmonic vibration mode. The anharmonicity of the vibration mode is obvious. (c) Atomic configurations showing the relationship between atomic vibration and large voids. The arrows indicate the vibration directions of the actively participating atoms. The length of the arrows is proportional to the amplitude of the eigenvector components of the atom.

potential energy actually decreases when they leave their balanced positions. While they may have a tendency to move toward the "pseudo energy minima" in Fig. 20a, they are restrained by the surrounding environment and have a weak restoring force. The results also reveal that this group of atoms is located between double-well-like partial potential energy minima. For the maximally active atom, the distance between the two partial potential energy minima is 1.8–2.0 Å. To inspect their involvement with voids, the eigenvector directions as well as the structural arrangement of the atoms involved in the softest mode are shown in Fig. 14b. It is immediately obvious that the vibration directions of these atoms always point toward or away from large voids. In other words, those atoms are LP atoms by definition. This phenomenon is common to all six low-frequency modes we examined. The particular atomic environment of the active atoms only requires minimal positional arrangements of nonactive atoms and does not cause steep energy rise due to the existence of large voids, explaining the anharmonicity of these vibrational modes.

Therefore, low-frequency vibrational modes are localized on LP atoms that are adjacent to the voids in MGs. Upon thermal excitation, the atomic environment of the LP atoms may undergo transient changes by jumping to and from the adjacent voids. This is consistent with the finding of Guerdane and Teichler[128] that a characteristic peak was observed on the frequency spectrum of local environment transition in a model MG. Experimental studies on the specific heat of bulk metallic glasses[35] may lend support to the view that loose packing is the origin of the excess vibrational modes. Along this direction, it would be possible to investigate how atomic packing efficiency, structural ordering, and void concentration affect the intensity of the BP and the fragile/strong behavior[62,113,129] among other properties of MGs.

ATOMIC DIFFUSION MECHANISMS AND STRUCTURAL DEFECTS

The mechanism for atomic diffusion in metallic glasses has been another long-standing problem.[130] Different from diffusion mechanisms in crystalline metals, where diffusion happens via vacancies and interstitials, diffusion in metallic glasses often involves thermally activated highly collective atomic processes.[131] Recent experiments[132] suggest that there are two distinct processes, namely single-atom hopping and collective motion, which contribute to long-range transport in the supercooled liquid state, with the latter being the dominant process. The exact micromechanisms for diffusion in metallic glass and factors that affect the diffusion mechanisms remain unclear.

At low temperatures, atoms are trapped in local potential wells; atom transport requires thermal activation to overcome the energy barriers. Therefore, atomic diffusion in glasses is essentially a barrier-crossing problem. In the following, we first study energy barriers required for atomic diffusion in MGs with different levels of structural ordering to reveal how structural order affects energy diffusion barriers. We then explore the correlations between structural defects and atomic transport mechanisms.

Diffusion Energy Barriers and Structural Ordering

The recently proposed activation-and-relaxation (ART) method[65] was used to sample the local regions of the PES and search for the saddle points around the glass IS. The saddle points are stationary points on the PES except the local minima (see Fig. 4). (A saddle point of order 1 is defined as a stationary point where only one of the eigenvalues of the Hessian matrix is negative.) Saddle points often define the transition-state structures on the minimum-energy path of the structural transformation. Computationally, saddle points are very difficult to locate because the number of saddle points grows exponentially with the number of particles in the system and they are related to initial paths departing from the local energy minima. The ART technique provides an efficient way to search for the saddle points, which involves three basic steps, i.e., leaving the harmonic potential basin following a randomly generated direction, converging to a saddle point by minimizing tangential forces along the inverse steepest descent path, and then leaving the saddle point to a new energy minimum. The method has been used to study diffusion problems in amorphous silicon and LJ model glasses.[65,133]

We sampled 50 configurations for both the IS_G and IS_L MGs using the 2024-atom ensemble under the constant-volume condition. For each IS we launched 200 barrier-crossing events (with different directions leaving the potential well). During the transition-state search, the sampling parameters for ART were optimized and remained the same for all events. Figure 21 displays the distribution of uphill energy barriers for the two glasses IS_G and IS_L. The barrier height is the energy difference between the saddle point and the potential minima for the whole system. For IS_G, the activation energy has a wide spectrum ranging from 0 eV to 2.5 eV, which can be described by a Gaussian fit with mean energy barrier of 1.27 eV. Experimental data on the diffusion barrier of Ni-P are unavailable, but the activation energy seems to fall within the range of typical MGs (1–4 eV).[132] Empirically, the activation energy barrier was found to be related to the glass-transition temperature as:[134–136]

$$E_\beta = 26.8RT_g, \tag{10}$$

where E_β is the energy barrier, R is the gas constant, and T_g is the glass-transition temperature. Plugging in the glass-transition temperature of the Ni-P glass from Fig. 1, we obtain the energy barrier as 1.31 eV, which is in surprisingly good agreement with the data we obtained using the ART technique.

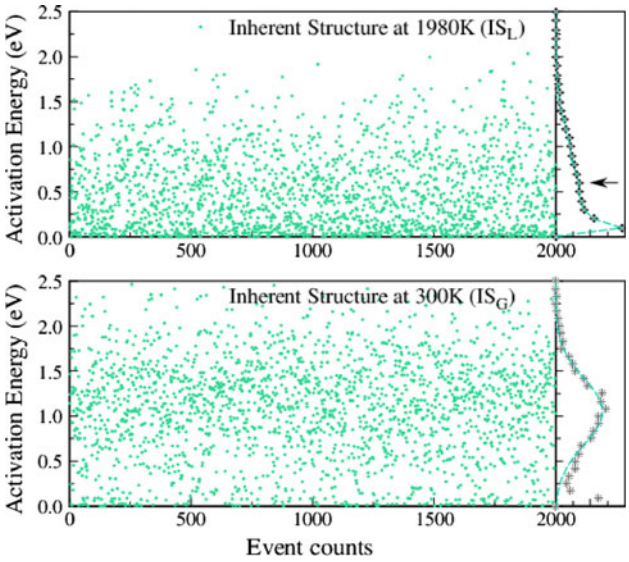

Fig. 21. Top panel: uphill energy barrier heights for different barrier-crossing events of the IS_L glass, and the energy barrier distribution. The line is a guide to the eye. Bottom panel: uphill energy barrier height for different barrier-crossing events for IS_G glass, and the energy barrier distribution. The line is a Gaussian fit to the distribution.

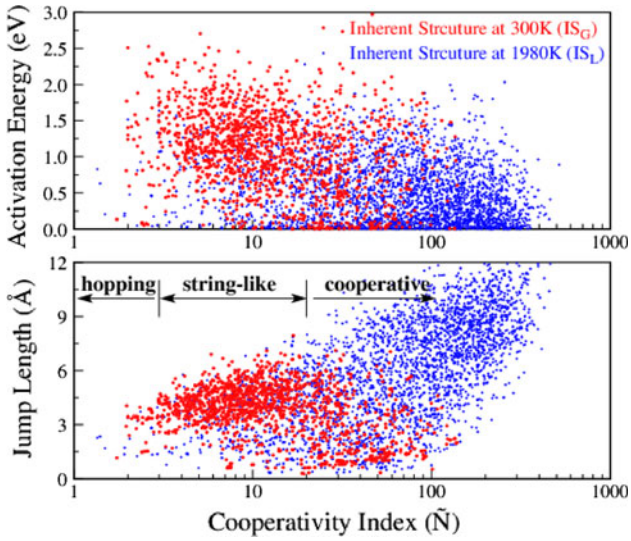

Fig. 22. Top panel: activation energy as a function of cooperativity index for both the IS_G and the IS_L configurations. Bottom panel: jump length as a function of cooperativity index for the IS_G and IS_L configurations.

By contrast, the energy distribution for IS_L is much more scattered, with a substantial amount of low-lying energy barriers. The center of gravity of the energy distribution clearly shifts toward low energy. As in Ref. 62, the distribution may be fitted with two or more Gaussians, and the mean activation value for the high-energy Gaussian is around 0.6 eV. This value is significantly lower than that of IS_G, and this result supports Sastry et al.'s finding[61] that at high temperatures the system explores a part of the landscape with low barriers between energy minima; at lower temperatures it explores minima with substantially higher energy barriers. Due to the drastic difference in the energy barrier between IS_L and IS_G, it is it evident that structural ordering/relaxation plays a significant role in governing atomic transport properties. This again has to do with the atomic mechanism of diffusion where subatomic voids as the structural defects play a vital role.

Micromechanisms for Atomic Diffusion in Metallic Glasses

To test the microscopic mechanism for atomic diffusion, we adopted two measures to quantify atomic arrangements. The first measure is the configurational distance between two adjacent energy minima on the PES, which can be considered as the total jump length defined as

$$D = \sqrt{\sum_{i=1}^{N} \left|r_i^{\mathrm{F}} - r_i^{\mathrm{I}}\right|^2}, \qquad (11)$$

where r_i^{F} and r_i^{I} denote the position of atom i located at the final and initial positions. The second measure of the atomic rearrangement is the cooperativity index $\tilde{N}$, defined as[62]

$$\tilde{N} = \left(\sum_{i}^{N} \left|r_i^{\mathrm{F}} - r_i^{\mathrm{I}}\right|^2\right) \Big/ \sum_{i}^{N} \left|r_i^{\mathrm{F}} - r_i^{\mathrm{I}}\right|^4. \qquad (12)$$

The cooperativity index can be roughly interpreted as the number of atoms actively participating in the transition. Both jump lengths and the cooperativity index are plotted in Fig. 22 as a function of activation energy for the glasses IS_G and IS_L. Generally speaking, the total jump length for IS_G is shorter than that for IS_L, which may be related to the shallow but spread-out potential wells at the high-energy portion of the energy landscape. The activation energy seems to decrease with increasing cooperativity index. For the well-relaxed glass IS_G the cooperativity index is smaller than that for IS_L, indicating that fewer atoms are involved in the diffusion event.

Combining detailed structural analysis, we found that the diffusion pathways are closely related to the number of atoms that participate in activation. Typical configuration changes along the transition pathways are shown in Fig. 23. Based on the cooperativity index, several diffusion mechanisms can be identified, of which the characteristics are stated below.

Atomic Hopping ($\tilde{N} < 3$)

Activation is highly localized on one to three atoms. In this regime, while the main mechanism can be characterized as atomic hopping, whose total jump length is small and activation energy is relatively high (>1 eV), several types of structural rearrangements coexist and they have different

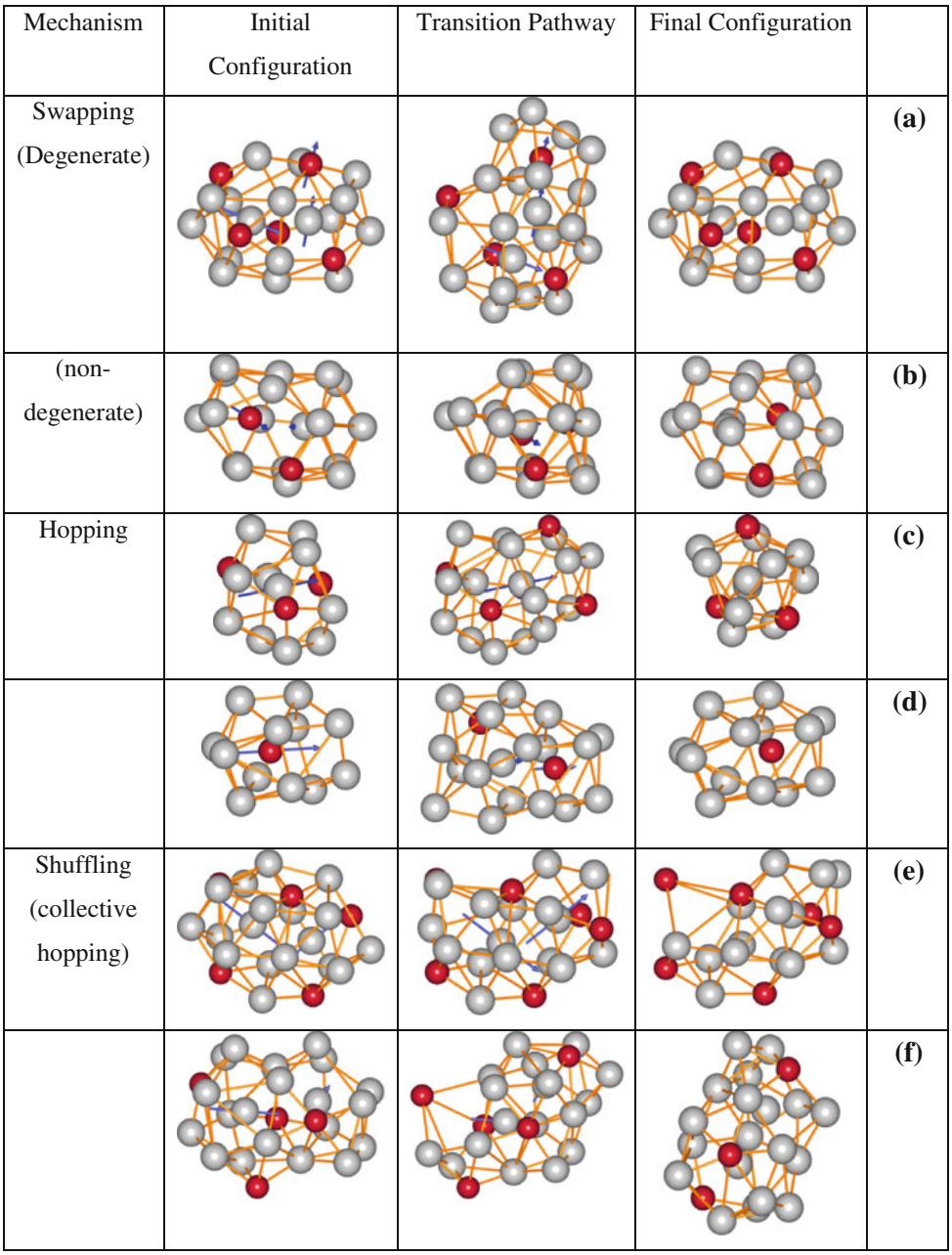

Fig. 23. Structural rearrangements illustrating different diffusion mechanisms for $\tilde{N} < 3$. The atoms with arrows are the ones actively participating in the movement. For each event, the configurations corresponding to the initial state (energy minimum), transition state (saddle point), and final state (energy minimum) are given. Structural changes can be observed by comparing the initial configuration and the final configuration.

characteristic activation energies. These structural arrangements can be described as:

1. Degenerate and nondegenerate atomic position swapping. In this case, the total jump length is large and the activation energy is high (>2.0 eV). Degenerate configurations involving three atoms were also found, but with slightly lower activation energies.
2. Atomic hopping involving one or two atoms. In this case, atoms jump from one cage to the next, involving obvious atomic coordination changes. In this diffusion mechanism, large cavities made individual atomic hopping possible. These jumps are favored near large voids which can accommodate them more readily. For atomic jumps involving cage-breaking (as shown in Fig. 23d), the activation energy is found to be 1.0–1.5 eV, close to the average activation energy of the system. In cases where atoms move within an oversized cage due to the existence of voids (Fig. 23e), or jump to an open space within the coordination shell, the energy cost is usually

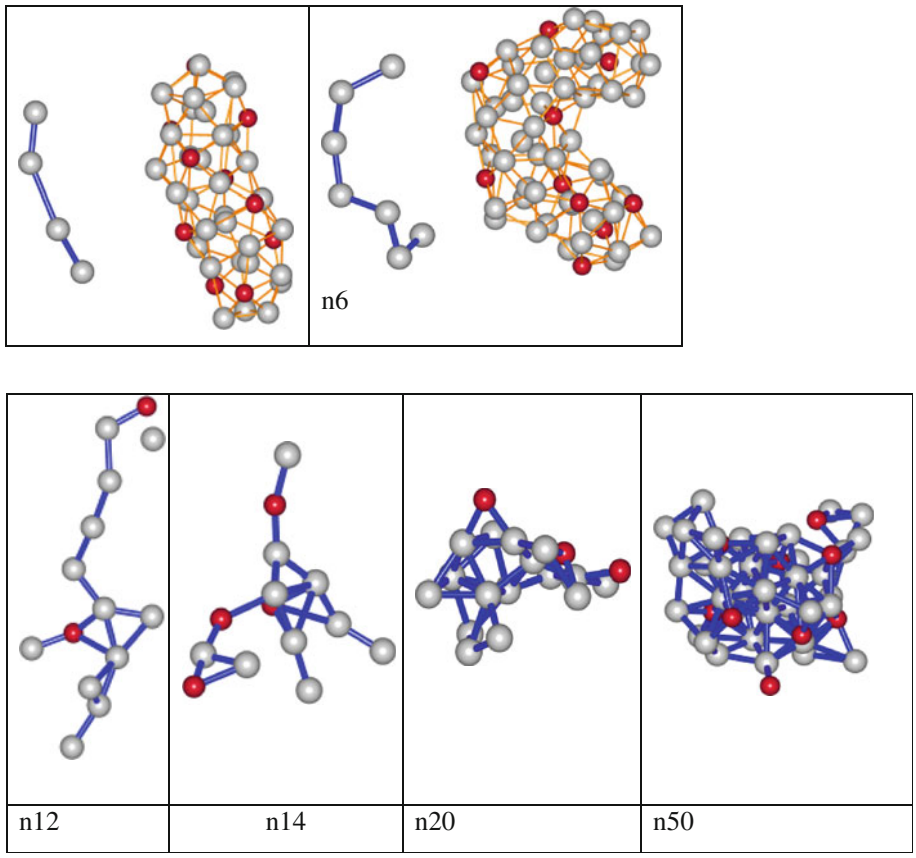

Fig. 24. Typical configurations of the string (n4, n6), string-like (n12, n14), and cooperatively rearranging (n20, n50) mechanisms for atomic diffusion.

small (<0.5 eV). In previous work on BMLJ, similar arrangements were categorized as nondiffusive structural arrangements by Middleton and Wales[62] However, in our view, since this type of arrangement involves bond breaking and bond formation, it should be considered as atomic hopping.

3. Atomic shuffling (collective hopping). Very often, the hopping event is accompanied by the jump of a second atom in the neighborhood to fill the empty space, forming paired atomic hopping, as shown in Fig. 23f.

String-to-String-Like ($3 < \tilde{N} < 20$)

In this regime, the diffusion mechanism changes from string to ramified string-like arrangement as the cooperativity index increases (Fig. 24). For small participation numbers (e.g., $\tilde{N} < 10$) the atomic movement can be described as string motions with 3–10 atoms participating in the motion. The one-dimensional string motion can be regarded as an extended hopping mechanism. In this mechanism, the most active atom typically has a jump length of ~2 Å, and the rest of the atoms participating in the diffusion have a fraction of the interatomic distance. Typical configurations for the string arrangement are shown in Fig. 24 (n4 and n6). With more atoms participating in the activation process, the string shape becomes more involved. More atoms near the diffusion path show structural adjustments, each with a nonnegligible displacement. The shape becomes more ramified as the cooperativity index increases, as shown in Fig. 24 (n12 and n14), where the most active atom induces two or three connected short chains. In previous computational work, local jumps were reported where groups of ten or more atoms move collectively, forming chainlike structures.[131,137] It is interesting to note that, in supercooled liquids, string-like atomic diffusion has been predicted by computer simuation[138,139] and experimentally observed in a colloidal system.[140] The string-like diffusion mechanism in metallic glasses has yet to be experimentally examined.

Cooperatively Rearranging ($\tilde{N} > 20$)

Structural relaxation with large cooperativity index is now extended to more atoms, and the shape of the structural rearrangement becomes spatially compact (as opposed to the ramified or fractal shapes mentioned above). The compact shape indicates that cooperative structural rearrangements involve a large number of atoms with each of them

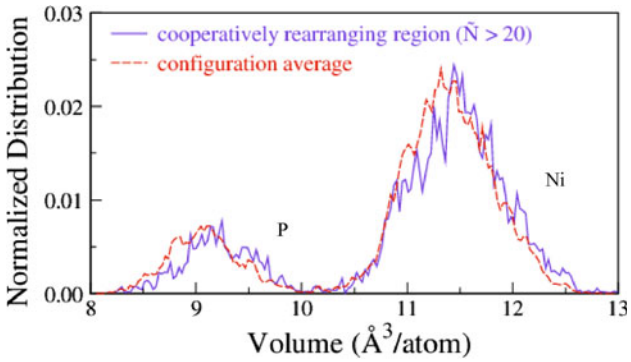

Fig. 25. Specific volumes of the cooperatively rearranging regions in comparison with the average specific volume of the full system. The density of the cooperatively rearranging zone is found to be 3.5% lower than the average atomic density of the system.

contributing similarly to the total jump length (i.e., a small fraction of the interatomic distance). For the well-relaxed glass (IS_G), the activation may involve up to ~120 atoms (~1.5 nm in diameter). It also shows signs of activation energy decrease for large cooperatively rearranging motions. For the unrelaxed IS_L glass, we find that the size of the cooperatively rearranging regions increases and the activation energy is lowered. These cooperatively rearranging zones bear connections to the concept of "entropy" droplets in the random first-order transition theory.[141,142]

The role of voids in controlling the diffusion mechanisms was further investigated. For large-$\tilde{N}$ cooperatively rearranging activities, to demonstrate that the activation zones are low-density zones with LP atoms, we evaluated the specific volume of the activation zone by summing up the atomic volumes of all participating atoms in the zone with $\tilde{N} > 20$ as shown in Fig. 21 (for the IS_G glass), and compared the volume with the average volume of the sample. The results are shown in Fig. 25. It is evident that the atoms in activation zones have larger atomic volumes than the average atomic volume of the sample, indicating that the cooperatively rearranging regions are low-density regions with more LP atoms. This is in agreement with Fig. 21, where the apparent energy barrier for the unrelaxed MG is much smaller. Clearly, the diffusion activation energy as well as the diffusion mechanisms are related to the content of the structural defects present in the glass and are sensitive to sample preparation history.

MECHANICAL PROPERTIES AND STRUCTURAL DEFECTS

By analyzing the vibrational property via normal mode analysis and atomic diffusion mechanism via barrier-crossing analysis, we quantified the local regions of the energy landscape of a model MG, and provided fundamental understanding of the connection between structure and energy landscape.

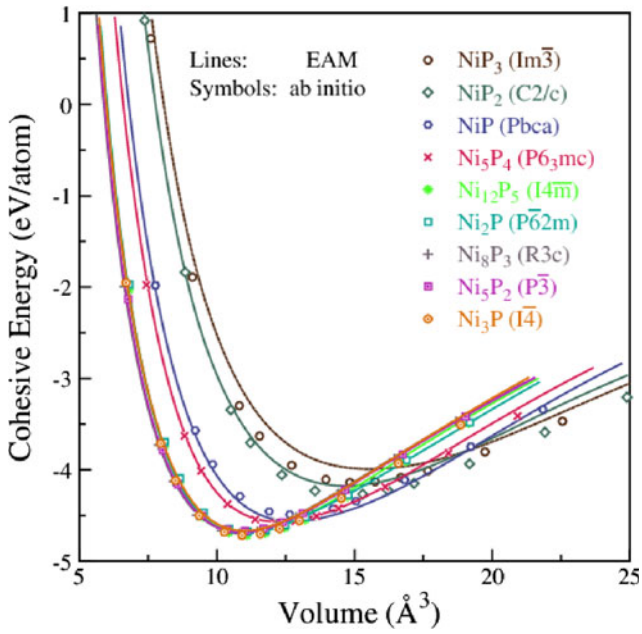

Fig. 26. Comparison of the cohesive energies of different crystalline compounds from ab initio and EAM calculations.

Certainly there are other very important properties of MGs that we are interested in but are unable to cover in this article. One particularly important property is the mechanical behavior of metallic glasses, which has been under intense research for many years.[7,143]

In metallic glasses, due to the lack of periodic lattice arrangement, the dislocation theory for crystal deformation is not applicable. Currently, one prevailing theory for the deformation of metallic glasses is one involving shear transformations[144,145] proposed by Argon, where the carrier of plasticity is localized in shear transformation zones (STZ) involving a group of atoms. One particularly important aspect of this theory is the initiation process of the STZs, which may dictate the overall mechanical behavior of MGs. It is thus crucial to understand (1) why there are STZs, and (2) how the STZs operate in MGs. The first question concerns the local structure of MGs. Theory and computational work has utilized the concepts of free volume, imperfect SRO, fertile sites, liquid-like (loose) packing, stiffness fluctuation, etc.,[7] suggesting that shear transformation preferentially nucleates from more disordered regions. While a quantitative and unified microscopic picture for STZs is still being sought, the knowledge of atomic packing defects discussed in this article may deepen our understanding of STZs. It is highly possible that the LP atoms, which are adjacent to subatomic voids resulting from cluster packing of irregular polyhedra, are the fertile sites for initiation of shear transformations due to their special properties discussed in "Properties of Voids and LP Atoms" section. The activation mechanism of shear transformation concerns the size of the STZ,

structural rearrangements within the STZ, and the energy barrier for the activation. The activation of STZs has been linked to thermal beta-relaxation before,[146–148] and a mechanism such as the cooperative shear model (CSM) has been proposed. In fact, the micromechanism for shear transformation can be studied by analyzing the free energy (potential energy plus strain energy) landscape of the system, featuring the disappearance of the basin of attraction under external stress. Mechanical activation barriers can be computatonally[149,150] resolved based on the external strain energy injected into the system. For mechanically induced activation processes, we predict that mechanical activation mechanisms are highly correlated with the atomic transport studied in "Atomic Diffusion Mechanisms and Structural Defects" section. There should exist a number of activation processes in addition to STZs, including the atomic jump mechanism proposed by Spaepen.[40,41] Since those events will have a wide distribution of activation energy barriers, the exact activation probabilities of the events (such as atomic jumps and STZs) are dependent on their thermodynamic distribution. It is likely that the CSMs are the dominant process under external stress because of their low activation energies. For all mechanically driven relaxation processes, we believe that structural defects such as voids, as a result of cluster packing, will dominate the initiation of shear transformations and/or atomic jumps.

CONCLUSIONS

We conducted computer simulations on a prototype metallic glass and demonstrated the concept of quasi-equivalent cluster packing in MGs. A substantial amount of voids exist in the glass as a result of short- to medium-range structural ordering. The geometric distribution and properties of the voids were characterized and used as an important quantity to correlate the atomic structure of metallic glasses with their dynamic properties. In particular, we revealed how vibrational and atomic transport properties are related to structural defects.

For the vibrational properties of this glass, a microscopic picture was provided to interpret the origin of the anomalous BP in the vibration spectrum. It was found that the long tail at the high-energy end of the VDOS spectrum is related to cluster packing on the medium range due to cage rattling of solute atoms. By analyzing the spatial correlation and participation contribution from the voids, we demonstrate that large voids in metallic glasses are the origin of the BP. For atomic transport properties, by conducting transition-state search on the PES of the MG, we revealed that the energy barrier for diffusion is profoundly affected by the level of structural ordering in the system. Further, micromechanisms for atomic transport in MGs were uncovered, including atomic hopping, string-like, and cooperatively rearranging structural arrangements. In all cases, the distribution of sub-atomic voids is found to be a very important factor controlling the diffusion mechanisms.

ACKNOWLEDGEMENTS

This work was supported by US NSF under Grant No. DMR-0907325 and ONR under Grant No. N00014-09-1-1025A. The work at Ames Laboratory was supported by the United States Department of Energy (USDOE), Office of Science (OS), Office of Basic Energy Science (BES), under Ames Laboratory Contract No. DE-AC02-07CH11358. E. Ma is supported by the US National Science Foundation, Division of Materials Research, under Contract No. NSF-DMR-0904188. H.W.S. acknowledges the use of the supercomputing system at the Center for Computational Materials Science, Institute for Materials Research, Tohoku University.

APPENDIX

To resolve the structure of metallic glasses, and predict their complex phase behavior under certain thermodynamic conditions, we were inspired to build computational models that can accurately describe the systems. First-principles calculations based on density functional theory, as implemented in the VASP simulation package, were used to explore the phase space of Ni-P and establish a coarse-grained PES of the system. A wide range of atomic configurations were selected, with each configuration containing typically more than 100 atoms. Of particular importance in constructing such a first-principles database is the selection of all crystalline phases existing in this alloy system as well as their derivative structures (defects, crystalline equation of state, heating trajectories, etc.). Nine crystallographic types of Ni-P intermetallic compounds were considered. Ab initio MD simulation was conducted on Ni-P alloys to obtain liquid structures and their trajectories along the supercooling process. All together, the configurations (~900 ab initio configurations) were used to form a first-principles database, including the potential energy and stress tensors of each configuration and forces on each atom, to quantitatively describe the Ni-P system. The database was further corrected to match experimental lattice parameters and cohesive energies of Ni and P. The as-generated first-principles database was used to parameterize the EAM potential for the Ni-P system using the potfit program,[56,151] with the goal of replicating the ab initio PES of Ni-P. During potential fitting, ad hoc EAM potentials were employed in classical MD to

probe deeper potential basins in the PES, and new configurations were added to the previously built potential database for a new round of EAM parameterization. Several iterations were performed until self-consistency between ab initio and EAM calculations was reached.

To validate the potential, we first evaluated the energetics and equilibrium lattice parameters of various intermetallic compounds of Ni-P, which are deemed important in our subsequent simulation of the structural evolution during the glass formation. The potential energies of all the crystalline phases, calculated using both the EAM and ab initio treatments, are plotted in Fig. 26 as a function of volume. EAM calculations predict the correct ordering of the energies of the Ni-P compounds. The energy differences between EAM and ab initio calculations for the intermetallic compounds at the ground state are less than 0.03 eV. In general, the match between EAM potential and ab initio results is satisfactory. On the P-rich side, the difference between EAM and ab initio data is slightly larger, which is probably due to the fact that more directional P-P bonds form in those alloys. The average difference of the lattice parameters of all crystalline structures at 300 K is less than 0.2%, corresponding to volume difference of 1%. The results demonstrate the capability and accuracy of the as-developed potential in simulating the structure of intermetallic compounds. The accuracy of the potential in describing Ni-P metallic liquids and glasses was further validated by comparing the structure and properties of computer-generated metallic glasses against experimental data, some of which have been presented in the main text. The results show that the as-developed potentials may offer a new avenue to shed light on the structure and physics of real-world MGs.

The EAM potential for the Ni-P system can be downloaded from: https://sites.google.com/a/gmu.edu/eam-potential-database/Home/NiP.

REFERENCES

1. W. Klement, R.H. Willens, and P. Duwez, *Nature* 187, 869 (1960).
2. F. Spaepen and D. Turnbull, *Ann. Rev. Phys. Chem.* 35, 241 (1984).
3. A.L. Greer, *Science* 267, 1947 (1995).
4. C.A. Angell, *Science* 267, 1924 (1995).
5. W.L. Johnson, *MRS Bull.* 24, 42 (1999).
6. A.L. Greer and E. Ma, *MRS Bull.* 32, 611 (2007).
7. Y.Q. Cheng and E. Ma, *Prog. Mater. Sci.* 56, 379 (2011).
8. P.H. Gaskell, *Nature* 276, 484 (1978).
9. P.H. Gaskell, *J. Non-Cryst. Solids* 32, 207 (1979).
10. D.R. Nelson and F. Spaepen, *Solid State Phys.* 42, 1 (1989).
11. A. L. Greer, *Intermetallic Compounds—Principles and Practice*, vol 1, ed. J.H. Westbrook and R.L. Fleischer (New York: Wiley, 1995), pp. 731–754.
12. F.C. Frank, *Proc. R. Soc. Lond. A* 215, 43 (1952).
13. S. Sachdev, *Bond Orientational Order in Condensed Matter Systems*, ed. K.J. Strandburg (New York: Springer-Verlag, 1992).
14. K.F. Kelton, et al., *Phys. Rev. Lett.* 90, 195504 (2003).
15. W.K. Luo, H.W. Sheng, and E. Ma, *Appl. Phys. Lett.* 89, 131927 (2006).
16. H.W. Sheng, et al., *Nature* 439, 419 (2006).
17. D.B. Miracle, *Nat. Mater.* 3, 697 (2004).
18. D.B. Miracle, *Acta Mater.* 54, 4317 (2006).
19. J. Ding, Y.Q. Cheng, H.W. Sheng, and E. Ma, *Phys. Rev. B* 85, 060201 (2012).
20. P.H. Gaskell, *J. Non-Cryst. Solids* 75, 329 (1985).
21. D.B. Miracle, W.S. Sanders, and O.N. Senkov, *Philos. Mag.* 83, 2409 (2003).
22. K.W. Park, J. Jang, M. Wakeda, Y. Shibutani, and J.-C. Lee, *Scr. Mater.* 57, 805 (2007).
23. V. Molinero, S. Sastry, and C.A. Angell, *Phys. Rev. Lett.* 18, 075701 (2006).
24. D. Ma, A.D. Stoica, X.-L. Wang, Z.P. Lu, M. Xu, and M. Kramer, *Phys. Rev. B* 80, 014202 (2009).
25. P. Panissod, D. Alliaga Guerra, A. Ammamou, J. Durand, and W.L. Johnson, *Phys. Rev. Lett.* 44, 1465 (1980).
26. I. Vincze, D.S. Boudreaux, and M. Tegze, *Phys. Rev. B* 19, 4896 (1979).
27. T.M. Hayes, J.W. Allen, J. Tauc, B.C. Giessen, and J.J. Hauser, *Phys. Rev. Lett.* 40, 1282 (1978).
28. X.K. Xi, B. Zhang, W.H. Wang, and Y. Wu, *Phys. Rev. Lett.* 99, 095501 (2007).
29. H.S. Chen, *Rep. Prog. Phys.* 43, 353 (1980).
30. T. Egami, *Ann. NY Acad. Sci.* 371, 238 (1981).
31. J. Eckert and A. Slipenyuk, *Scr. Mater.* 50, 39 (2004).
32. H. Beck and H.-J. Güntherodt, *Glassy Metals II: Atomic Structure and Dynamics, Electronic Structure, Magnetic Properties* (New York: Springer, 1983).
33. A.R. Yavari, A. Le Moulec, A. Inoue, N. Nishiyama, N. Lupu, E. Matsubara, W.J. Botta, G. Vaughan, M. Di Michiel, and A. Kvick, *Acta Mater.* 53, 1611 (2005).
34. T. Ichitsubo, E. Matasubara, T. Yamamoto, H.S. Chen, N. Nishiyama, J. Saida, and K. Anazawa, *Phys. Rev. Lett.* 95, 245501 (2005).
35. Y. Li, H.Y. Bai, W.H. Wang, and K. Samwer, *Phys. Rev. B* 74, 052201 (2006).
36. T. Ichitsubo, S. Hosokawa, K.K. Matsuda, E. Matsubara, N. Nishiyama, S. Tsutsui, and A.Q.R. Baron, *Phys. Rev. B* 76, 140201(R) (2007).
37. T. Fujita, K. Konno, W. Zhang, V. Kumar, M. Matsuura, A. Inoue, T. Sakurai, and M.W. Chen, *Phys. Rev. Lett.* 103, 075502 (2009).
38. D. Turnbull and M.H. Cohen, *J. Chem. Phys.* 34, 120 (1961).
39. M.H. Cohen and G.S. Grest, *Phys. Rev. B* 20, 1077 (1979).
40. F. Spaepen, *Acta Metall.* 25, 407 (1977).
41. F. Spaepen, *Scr. Mater.* 54, 363 (2006).
42. Y.H. Liu, D. Wang, K. Nakajima, W. Zhang, A. Hirata, T. Nishi, A. Inoue, and M.W. Chen, *Phys. Rev. Lett.* 106, 125504 (2011).
43. H. Wagner, D. Bedorf, S. Kuchemann, M. Schwabe, B. Zhang, W. Arnold, and K. Samwer, *Nat. Mater.* 10, 439 (2011).
44. L. Tian, Y.Q. Cheng, Z.W. Shan, J. Li, C.C. Wang, X.D. Han, J. Sun, and E. Ma, *Nat. Commun.* 3, 609 (2012).
45. W. Kauzmann, *Chem. Rev.* 43, 219 (1948).
46. P.G. Debenedetti and F.H. Stillinger, *Nature* 259, 410 (2010).
47. T. Egami, T.K. Maeda, and V. Vitek, *Philos. Mag. A* 41, 883 (1980).
48. D. Srolovitz, K. Maeda, V. Vitek, and T. Egami, *Philos. Mag. A* 44, 847 (1981).
49. V. Vitek and T. Egami, *Phys. Status Solidi B* 144, 145 (1987).
50. T. Egami, *Prog. Mater. Sci.* 56, 637 (2011).
51. C. Hausleitner and J. Hafner, *Phys. Rev. B* 45, 128 (1992).
52. C. Hausleitner and J. Hafner, *Phys. Rev. B* 47, 5689 (1993).
53. M.S. Daw and M.I. Baskes, *Phys. Rev. Lett.* 50, 1285 (1983).
54. M.S. Daw and M.I. Baskes, *Phys. Rev. B* 29, 6443 (1984).
55. F. Ercolessi and J.B. Adams, *Europhys. Lett.* 26, 583 (1994).
56. H.W. Sheng, M.J. Kramer, A. Cadien, T. Fujita, and M.W. Chen, *Phys. Rev. B* 83 (13), 134118 (2011).
57. G. Kresse and J. Furthmuller, *Phys. Rev. B* 54, 11169 (1996).
58. G. Kresse and D. Joubert, *Phys. Rev. B* 59, 1758 (1999).

59. Y.Q. Cheng, E. Ma, and H.W. Sheng, *Phys. Rev. Lett.* 102, 245501 (2009).
60. W. Kob and H.C. Andersen, *Phys. Rev. E* 51, 4626 (1995).
61. S. Sastry, P.G. Debenedetti, and F.H. Stillinger, *Nature* 393, 554 (1998).
62. T.F. Middleton and D.J. Wales, *Phys. Rev. B* 64, 024205 (2001).
63. D. Coslovich and G. Pastore, *J. Chem. Phys.* 127, 124504 (2007).
64. A. Heuer, *J. Phys. Condens. Matter* 20, 373101 (2008).
65. G.T. Barkema and N. Mousseau, *Phys. Rev. Lett.* 77, 4358 (1996).
66. J.R. Hernandez and P. Harrowell, *Phys. Rev. E* 67, 011403 (2003).
67. J.R. Hernandez and P. Harrowell, *J. Chem. Phys.* 120, 9222 (2004).
68. J. Swetlana and D. Christoph, *J. Chem. Phys.* 134, 104501 (2011).
69. R. Harris and L.J. Lewis, *Phys. Rev. B* 25, 4997 (1982).
70. T.A. Webber and F.H. Stillinger, *Phys. Rev. B* 32, 5402 (1985).
71. W.Y. Ching, *Phys. Rev. B* 34, 2080 (1986).
72. I.-R. Lu, G. Wlide, G.P. Gorler, and R. Willnecker, *J. Non-Cryst. Solids* 250–252, 577 (1999).
73. K. Lu, J.T. Wang, and W.D. Wei, *J. Phys. D* 25, 808 (1992).
74. H.S. Chen, J.T. Krause, and E. Coleman, *J. Non-Cryst. Solids* 18, 157 (1975).
75. K. Lu and J.T. Wang, *Mater. Sci. Eng.* A133, 500 (1991).
76. G.S. Cargill, *J. Appl. Phys.* 41, 12 (1970).
77. V.P. Voloshin, Y.I. Naberukhin, and N.N. Medvedev, et al., *J. Chem. Phys.* 102, 4981 (1995).
78. P. Lamparter, *Phys. Scr.* T57, 72 (1995).
79. W.K. Luo and E. Ma, *J. Non-Cryst. Solids* 354, 945 (2008).
80. H.W. Sheng, H.Z. Liu, Y.Q. Cheng, J. Wen, P.L. Lee, W.K. Luo, S.D. Shastri, and E. Ma, *Nat. Mater.* 6, 192 (2007).
81. F.C. Frank and J.S. Kasper, *Acta Crystallogr.* 11, 184 (1958).
82. F.C. Frank and J.S. Kasper, *Acta Crystall.* 12, 483 (1959).
83. B.E. Warren, *X-ray Diffraction* (New York: Dover, 1990).
84. R. Harris and L.J. Lewis, *J. Phys. F* 13, 1359 (1983).
85. J.L. Finney, *Proc. R. Soc. Lond. A* 319, 479 (1970).
86. J.L. Finney, *Proc. R. Soc. Lond. A* 319, 495 (1970).
87. T. Egami and Y. Waseda, *J. Non-Cryst. Solids* 64, 113 (1984).
88. R. Skala and M. Drabek, *Miner. Mag.* 67, 783 (2003).
89. M. Goldstein, *J. Chem. Phys.* 51, 3728 (1969).
90. F.H. Stillinger, *Science* 267, 1935 (1995).
91. D. Wales, *Energy Landscapes: Applications to Clusters, Biomolecules and Glasses, Cambridge Molecular Science* (Cambridge: Cambridge University Press, 2004).
92. P.J. Steinhardt, D.R. Nelson, and M. Ronchetti, *Phys. Rev. B* 28, 784 (1983).
93. A.S. Clarke and H. Jónsson, *Phys. Rev. E* 47, 3975 (1993).
94. R.M. Ernst, S.R. Nagel, and G.S. Grest, *Phys. Rev. B* 43, 8070 (1991).
95. C. Dasgupta, A. Indrani, S. Ramaswamy, and M.K. Phani, *Europhys. Lett.* 15, 307 (1991).
96. J.D. Bernal, *Proc. R. Soc. Lond. A* 280, 299 (1964).
97. E.J.W. Whittaker, *J. Non-Cryst. Solids* 28, 293 (1978).
98. H.J. Frost, *Acta Metall.* 30, 889 (1982).
99. V.P. Voloshin and YuI Naberukin, *J. Phys. Condens. Matter* 5, 5685 (1993).
100. J. Harris, *Phys. Rev. B* 31, 1770 (1985).
101. A. Bharathula, et al., *Metal. Mater. Trans. A* 39, 1779 (2008).
102. S. Sastry, D.S. Corti, and P.G. Debenedetti, et al., *Phys. Rev. E* 56, 5524 (1997).
103. J. Sietasma and B.J. Thijsse, *Phys. Rev. B* 52, 3248 (1995).
104. M.O. Steinhauser, *J. Chem. Phys.* 122, 094901 (2005).
105. K.M. Flores, E. Sherer, and A. Bharathula, et al., *Acta Mater.* 55, 3403 (2007).
106. Y.F. Shi and M.L. Falk, *Phys. Rev. Lett.* 95, 095502 (2005).
107. Y.Q. Cheng and E. Ma, *Appl. Phys. Lett.* 93, 051910 (2008).
108. Y.Q. Cheng, H.W. Sheng, and E. Ma, *Phys. Rev. B* 78, 014207 (2008).
109. W.A. Phillips, eds., *Amorphous Solids: Low-Temperature Properties* (New York: Springer, 1981).
110. K. Rice and H.C. Ramsperger, *J. Am. Chem. Soc.* 49, 1617 (1927).
111. R. Zwanzig, *J. Chem. Phys.* 79, 4507 (1983).
112. U. Buchenau, M. Prager, N. Nucker, A.J. Dianoux, N. Ahamad, and W.A. Phillips, *Phys. Rev. B* 34, 5665 (1986).
113. A.P. Sokolov, A. Kisliuk, M. Soltwisch, and D. Quitmann, *Phys. Rev. Lett.* 69, 1540 (1992).
114. C.A. Angell, *J. Non-Cryst. Solids* 131–133, 13 (1991).
115. B.B. Laird and H.R. Schober, *Phys. Rev. Lett.* 66, 636 (1991).
116. S. Taraskin and S. Elliott, *Europhys. Lett.* 39, 37 (1997).
117. S.N. Taraskin and S.R. Elliot, *Phys. Rev. B* 59, 8572 (1999).
118. H. Schober and C. Oligschleger, *Phys. Rev. B* 53, 11469 (1996).
119. V.A. Luchnikov, N.N. Medvedev, Y.I. Naberukin, and H.R. Schober, *Phys. Rev. B* 62, 3181 (2000).
120. H. Shintani and H. Tanaka, *Nat. Mater.* 7, 870 (2008).
121. S. Mentese, J.B. Suck, and V. Read, *Appl. Phys. A* 74, s969 (2002).
122. P.M. Derlet, R. Maaβ, and J.F. Loffler, *Mater. Mes. Soc. Symp. Proc.* 1224, GG05-01 (2010).
123. K. Suzuki, K. Shibata, and H. Mizuseki, *J. Non-Cryst. Solids* 156, 58 (1993).
124. R. Caciuffo, O. Francescangeli, and S. Melone, et al., *J. Phys. Condens. Matter* 1, 5621 (1989).
125. P. Ballone and S. Rubini, *Phys. Rev. B* 51, 14962 (1995).
126. J. Hafner and M. Krajci, *J. Phys. Condens. Matter* 6, 4631 (1994).
127. V. Mazzacurati, G. Ruocco, and M. Sampoli, *Europhys. Lett.* 34, 681 (1996).
128. M. Guerdane and H. Teichler, *Phys. Rev. Lett.* 101, 065505 (2008).
129. M. Plazanet and H. Schober, *Phys. Chem. Chem. Phys.* 10, 5723 (2008).
130. A.L. Greer, *J. Non-Cryst. Solids* 61, 737 (1984).
131. F. Faupel, W. Frank, M.P. Macht, H. Mehrer, V. Naundorf, K. Ratzke, H.R. Schober, S.H. Sharma, and H. Teichler, *Rev. Mod. Phys.* 75, 273 (2003).
132. X.P. Tang, U. Geyer, R. Busch, W.L. Johnson, and Y. Wu, *Nature* 402, 160 (1999).
133. D. Rodney and T. Schroder, *Euro. Phys. J. E* 34, 100 (2011).
134. K.L. Ngai and S. Capaccioli, *Phys. Rev. E* 69, 031501 (2004).
135. Z.F. Zhang, P. Wen, C.H. Shek, and W.H. Wang, *Phys. Rev. B* 75, 174201 (2007).
136. L.N. Hu and Y.Z. Yue, *J. Phys. Chem. C* 113, 15001 (2009).
137. C. Oligschleger and H.R. Schober, *Phys. Rev. B* 59, 811 (1999).
138. J.D. Stevenson, J. Schmalian, and P.G. Wolynes, *Nat. Phys.* 2, 268 (2006).
139. C. Donati, J.F. Douglas, W. Kob, S.J. Plimpton, P.H. Poole, and S.C. Glotzer, *Phys. Rev. Lett.* 80, 2338 (1998).
140. E.R. Weeks, J.C. Crocker, A.C. Levitt, A. Schofield, and D.A. Weitz, *Science* 287, 627 (2000).
141. M. Dzero, J. Schmalian, and P.G. Walynes, *Phys. Rev. B* 72, 100201 (2005).
142. X.Y. Xia and P.G. Wollynes, *Proc. Natl. Acad. Sci.* 97, 2990 (2000).
143. C.A. Schuh, T.A. Hufnagel, and U. Ramamury, *Acta Mater.* 55, 4067 (2007).
144. A.S. Argon, *Acta Metall.* 27, 47 (1979).
145. A.S. Argon, *J. Phys. Chem. Solids* 43, 945 (1982).
146. G.P. Johari and M. Goldstein, *J. Chem. Phys.* 53, 2372 (1970).
147. H.B. Yu, W.H. Wang, H.Y. Bai, Y. Wu, and M.W. Chen, *Phys. Rev. B* 81, 220201 (2010).
148. M.D. Demetriou, J.S. Harmon, M. Tao, G. Duan, K. Samwer, and W.L. Johnson, *Phys. Rev. Lett.* 97, 065502 (2006).
149. D. Rodney and C. Schuh, *Phys. Rev. Lett.* 102, 235503 (2009).
150. S.G. Mayr, *Phys. Rev. Lett.* 97, 195501 (2006).
151. P. Brommer and F. Gahler, *Modell. Simul. Mater. Sci. Eng.* 15, 295 (2007).